

**AN AVO METHOD TOWARD DIRECT DETECTION OF  
LITHOLOGIES COMBINING P-P AND P-S REFLECTION DATA**

A Thesis

by

JUAN RAMON DE JESUS CARCUZ JEREZ

Submitted to the Office of Graduate Studies of  
Texas A&M University  
in partial fulfillment of the requirements for the degree of  
MASTER OF SCIENCE

May 2003

Major Subject: Geophysics

AN AVO METHOD TOWARD DIRECT DETECTION OF  
LITHOLOGIES COMBINING P-P AND P-S REFLECTION DATA

A Thesis

by

JUAN RAMON DE JESUS CARCUZ JEREZ

Submitted to Texas A&M University  
in partial fulfillment of the requirements  
for the degree of

MASTER OF SCIENCE

Approved as to style and content by:

---

Luc T. Ikelle  
(Chair of Committee)

---

Richard L. Carlson  
(Member)

---

Daulat D. Mamora  
(Member)

---

Andrew Hajash Jr.  
(Head of Department)

May 2003

Major Subject: Geophysics

## ABSTRACT

An AVO Method toward Direct Detection of Lithologies Combining  
 $P - P$  and  $P - S$  Reflection Data. (May 2003)

Juan Ramon de Jesus Carcuiz Jerez, B.S., Texas A&M University

Chair of Advisory Committee: Dr. Luc T. Ikelle

I here present a combined AVO analysis of  $P - P$  and  $P - S$  reflection data whose objective is to improve the identification of lithology by estimating the specific values of Poisson's ratio,  $\sigma$ , for each rock formation in a given geological model, rather than a contrast between formations. Limited knowledge on the elastic parameters of a given rock formation and difficulty regarding the availability and processing of  $P - S$  data constitute hindrances of lithology identification. Considering that ocean bottom seismology (OBS) has aided in solving the problem of  $P - S$  data availability, limited information on elastic parameters is still a challenge, and the focus of this thesis.

The present analysis is based on Zoeppritz' solution for the  $P - P$  and  $P - S$  reflection coefficients,  $R_{PP}$  and  $R_{PS}$ , with a slight modification. We used the normalized  $P - S$  reflection coefficient; i.e.,

$$R'_{PS} = \frac{R_{PS}}{\sin \theta} \text{ for } \theta > 0 ,$$

instead of  $R_{PS}$ , where  $\theta$  is the incident angle. By normalizing  $R_{PS}$ , we avoid dealing with the absence of converted  $S$ -waves at small incident angles and enhance the similar linear behavior of the  $P - P$  and normalized  $P - S$  reflection coefficients at small angles of incidence.

We have used the linearity of  $R_{PP}$  and  $R'_{PS}$  at angles smaller than 35 degrees to simultaneously estimate the average  $V_P/V_S$  ratio, the contrasts of  $P$ - and  $S$ -wave

velocities, and the contrast of density. Using this information, we solve for Poisson's ratio of each formation, which may enable lithology discrimination. The feasibility of this analysis was demonstrated using nonlinear synthetic data (i.e., finite-difference data). The results in estimating Poisson's ratio yielded less than 5 percent error.

We generalize this new combined  $P - P$  and  $P - S$  AVO analysis for dipping interfaces. Similarly to the nondipping interface case, our derivations show that the amplitude variation with offset (AVO) of  $P - P$  and  $P - S$  for a dipping interface can be cast into intercepts and gradients. However, these intercepts and gradients depend on the angle of the dipping interface. Therefore, we further generalize our analysis by including a migration step that allows us to find the dipping angle.

Because seismic data is not available in terms of  $R_{PP}$  and  $R'_{PS}$ , this process includes recovery of reflection coefficients after migrating the data and correcting for geometrical spreading, as done by Ikelle et al. (1986 and 1988). The combination of all of these steps, namely geometrical-spreading correction, migration, and AVO analysis, is another novelty of this thesis, which leads to finding the specific values of Poisson's ratio of each rock formation directly from the seismic data.

To my mother Gloria Jerez, may I always follow your wisdom and make you proud.

## ACKNOWLEDGMENTS

I would like to thank Dr. Luc Ikelle. His endless teachings, guidance, and support have been fundamental to my growth as a professional scientist and researcher.

I would also like to express my gratitude to my committee members, Dr. Richard Carlson and Dr. Daulat Mamora, for their engaging comments and valuable time.

Thanks are also needed to all the former and current CASP members, who provided technical support and fond memories, as well as all the sponsors of the CASP project that made this and other research possible.

I would probably not be writing this if it were not for the unconditional support of my family. They taught me and showed me the value of unity and love. Along with my family I thank my friends who enrich my life day by day.

Finally and above all, I thank the Creator and Giver, my father God.

## TABLE OF CONTENTS

	Page
ABSTRACT . . . . .	iii
DEDICATION . . . . .	v
ACKNOWLEDGMENTS . . . . .	vi
TABLE OF CONTENTS . . . . .	vii
LIST OF TABLES . . . . .	x
LIST OF FIGURES . . . . .	xii
 CHAPTER	
I	
WHY SOLVING FOR POISSON’S RATIO: ACTUAL VALUE VERSUS CONTRAST . . . . .	1
1.1 Problem Description . . . . .	3
1.2 Previous Work . . . . .	3
1.3 Methodology . . . . .	4
1.4 Assumptions . . . . .	6
1.5 Novelty and Importance . . . . .	7
1.6 Scope of This Thesis . . . . .	9
1.6.1 AVO Analysis Combining $P - P$ and $P - S$ Data: A Nonlinear Inversion for Poisson’s Ratio .	10
1.6.2 An Application to Finite-Difference Simulations .	10
1.6.3 Analysis and Generalization for Dipping Interfaces	11
1.6.4 An Integrated Approach to Migration and AVO Inversion . . . . .	11

CHAPTER	Page	
II	AVO ANALYSIS COMBINING $P - P$ AND $P - S$ DATA: A NONLINEAR INVERSION FOR POISSON'S RATIO . . . . .	12
	2.1 Definition of Models . . . . .	12
	2.1.1 Normalization of $R_{PS}$ . . . . .	14
	2.1.2 Similarities and Differences Between $R_{PP}$ and $R'_{PS}$ . . . . .	14
	2.2 Small-Angle Linear Approximation . . . . .	17
	2.2.1 Linear Approximation Equations . . . . .	17
	2.2.2 Validation of Linear Approximations . . . . .	18
	2.2.3 Discussion . . . . .	20
	2.3 Nonlinear Inversion for Elastic Contrasts and $V_P/V_S$ . . . . .	20
	2.3.1 Objective . . . . .	20
	2.3.2 Inversion . . . . .	21
	2.3.3 Results . . . . .	22
	2.3.4 Discussion . . . . .	23
	2.4 Identification of Lithology . . . . .	25
III	AN APPLICATION TO FINITE-DIFFERENCE SIMULATIONS	27
	3.1 Introduction . . . . .	27
	3.2 Review of Finite-Difference Modeling . . . . .	27
	3.2.1 Elastic Wave Equations . . . . .	28
	3.2.2 Approximation . . . . .	29
	3.2.3 Implementation . . . . .	31
	3.2.4 Discussion . . . . .	34
	3.3 Inversion Algorithm . . . . .	35
	3.4 Model Description . . . . .	37
	3.4.1 $P - P/P - S$ Separation . . . . .	40
	3.4.2 Extraction of Reflection Coefficients . . . . .	41
	3.5 Inversion . . . . .	42
	3.5.1 Step 1: Linear Approximation . . . . .	45
	3.5.2 Step 2: Nonlinear Inversion . . . . .	45
	3.5.3 Step 3: Specific Poisson's Ratio . . . . .	47



CHAPTER	Page	
IV	ANALYSIS AND GENERALIZATION FOR DIPPING INTERFACES . . . . .	48
	4.1 Problems caused by dip . . . . .	49
	4.2 AVO Equations for Dipping Interfaces . . . . .	50
	4.2.1 $P - P$ Reflection . . . . .	52
	4.2.2 Normalized $P - S$ Reflection . . . . .	53
	4.3 Generalization of the AVO Equations . . . . .	54
	4.4 Consequences of Dipping Reflectors . . . . .	55
V	AN INTEGRATED APPROACH TO MIGRATION AND AVO INVERSION . . . . .	56
	5.1 Linearized Inversion . . . . .	57
	5.1.1 Forward Problem . . . . .	58
	5.1.2 Forward Problem in Elastic Media . . . . .	62
	5.1.3 Inversion for $f_{AVO}$ . . . . .	65
	5.2 Implementation . . . . .	66
	5.2.1 Model Description . . . . .	67
	5.2.2 Preliminary Results . . . . .	68
	5.3 Recommendations for Processing and Inversion of Data . . . . .	72
VI	CONCLUSIONS . . . . .	75
	REFERENCES . . . . .	77
	VITA . . . . .	81

## LIST OF TABLES

TABLE	Page
1.1	Poisson's ratio for common lithologies. . . . . 8
2.1	Elastic Parameters for four differing half-space models: unconsolidated shale/sand, shale/salt, gas shale/limestone, and limestone/salt [ $V_P$ : $P$ -wave velocity; $V_S$ : $S$ -wave velocity; and $\rho$ : density]. . . . . 14
2.2	Numerical values of the intercepts and gradients [ $A_{PP}$ : $R_{PP}$ intercept; $B_{PP}$ : $R_{PP}$ gradient; $A_{PS}$ : $R'_{PS}$ intercept; and $B_{PS}$ : $R'_{PS}$ gradient]. . . . . 18
2.3	Estimated and actual values of $\Delta V_P/V_P$ , $\Delta V_S/V_S$ , $\Delta\rho/\rho$ , and $V_P/V_S$ . The less-than-1-percent error of approximation between estimated and actual values shows the accuracy of the inversion process. . . . . 23
2.4	Estimated and actual values for the specific $(V_P/V_S)_k$ and Poisson's ratio for each layer in all models considered in this chapter. The estimated values approximate the actual ones with an error no greater than 1 percent. . . . . 26
3.1	Elastic parameters for an isotropic half-space similar to the shale/salt model from chapter II [ $V_P$ : $P$ -wave velocity; $V_S$ : $S$ -wave velocity; and $\rho$ : density]. . . . . 37
3.2	Intercepts and gradients [ $A_{PP}$ : $R_{PP}$ intercept; $B_{PP}$ : $R_{PP}$ gradient; $A_{PS}$ : $R'_{PS}$ intercept; and $B_{PS}$ : $R'_{PS}$ gradient] for the shale/salt model described in Table 3.1. . . . . 45
3.3	Estimated and actual values of $\Delta V_P/V_P$ , $\Delta V_S/V_S$ , $\Delta\rho/\rho$ , and $V_P/V_S$ for the shale/salt model used in this chapter. The less-than-1-percent error of approximation between estimated and actual values shows the accuracy of the inversion process. . . . . 46

TABLE	Page	
3.4	Estimated and actual values for the specific $(V_P/V_S)_k$ and Poisson's ratio for each layer in the shale/salt model considered in this chapter. The estimated values approximate the actual ones with an error no greater than 5 percent. . . . .	47
5.1	Elastic Parameters for a heterogeneous complex geological model [ $V_P$ : $P$ -wave velocity; $V_S$ : $S$ -wave velocity; $\rho$ : density; and $\sigma_k$ : Poisson's ratio]. . . . .	68

## LIST OF FIGURES

FIGURE	Page	
1.1	Problem to analyze: A half-space model where the elastic parameters of each media are $V_{P1}, V_{S1}, \rho_1, V_{P2}, V_{S2}$ , and $\rho_2$ , and two seismic events take place: reflection of $P$ -wave and its conversion into $S$ -wave. . . . .	6
2.1	$P - P$ (blue) and $P - S$ (red) reflection coefficients for the four models described in Table 2.1. There is not an obvious relationship between $R_{PP}$ and $R_{PS}$ , which we attribute to the nonlinear behavior of $R_{PS}$ . . . . .	13
2.2	$P - P$ (blue) and normalized $P - S$ (red) reflection coefficients for the four models described in Table 2.1. Now $R'_{PS}$ does behave similarly to $R_{PP}$ . At small angles, they run linearly with opposite gradient, they peak at the critical angle, and they drop down abruptly. $R'_{PS}$ is not defined at zero; thus this figure begins at an angle slightly greater than zero. . . . .	15
2.3	Different trends of reflection coefficient gradients: (a) opposite gradient towards each other. (b) opposite gradient away from each other. (c) both positive gradients. (d) both negative gradients. Only (a) is considered realistic. . . . .	17
2.4	Linear approximation (black) for the $P - P$ reflection coefficient (blue) and the normalized $P - S$ reflection coefficient (red), obtained from equations (2.2-2.7) for the four models described in Table 2.1. Because $R'_{PS}$ is not defined at zero, this figure begins at an angle slightly greater than zero. . . . .	19
2.5	Variation of the least-square cost function with values of the $V_P/V_S$ ratio for the models described in Table 2.1. Each figure displays only one minimum value. Hence it shows that system of equations (2.8-2.11) has a unique solution. . . . .	24

FIGURE	Page
3.1	Finite-difference staggered grid used to update the velocity and stress calculations (modified from Levander, 1988). . . . . 32
3.2	Accurate and complete isotropic model that leads from a seismic data input (i.e., $R_{PP}$ and $R'_{PS}$ ) to the specific values of Poisson's ratio ( $\sigma_i$ ) for each lithology forming an interface. . . . . 36
3.3	Geological model and aquisition geometry to input in finite-difference code. . . . . 38
3.4	Finite-difference generated seismic data showing: (a) Horizontal component of normal stress ( $\tau_{xx}$ ); (b) Divergence; and (c) Curl. . . . 39
3.5	$P - P$ reflection coefficient of the shale/salt model [(a) exact from Zoeppritz' solution (black); (b) estimated from seismic data (red); (c) approximated by equations 2.2-2.7 (blue); (d) compilation of (a), (b), and (c)]. . . . . 43
3.6	Normalized $P - S$ reflection coefficient of the shale/salt model [(a) exact from Zoeppritz' solution (black); (b) estimated from seismic data (red); (c) approximated by equations 2.2-2.7 (blue); (d) compilation of (a), (b), and (c)]. . . . . 44
3.7	Variation of the least-square cost function with values of the $V_P/V_S$ ratio for the shale/salt model described in Table 3.1. This figure displays only one minimum value. Hence it shows that the problem has a unique solution. . . . . 46
4.1	$P - P$ and $P - S$ reflection at different interfaces. (a) $P - P$ reflection on a flat interface, (b) $P - P$ reflection on a dipping interface, (c) $P - S$ reflection on a flat interface, and (d) $P - S$ reflection on a dipping interface. [ $\theta_S$ : the incident angle, $\theta_R$ : the reflection angle, $\theta_C$ : the converted $S$ -wave angle, $\theta$ : the total reflection angle, and $\theta'$ : the dipping angle.] . . . . . 51
5.1	Complex geological model and aquisition geometry to generate finite-difference data. . . . . 67

FIGURE	Page
5.2	$P - P$ and $P - S$ reflections recorded in the seismic data. . . . . 69
5.3	Finite-difference generated seismic data showing the horizontal component of normal stress ( $\tau_{xx}$ ) for the model shown in Figure 5.1 at different source locations: (a) 0m; (b) 400m; (c) 750m; (d) 1100m; and (e) 1500m. . . . . 70
5.4	$P - P$ and $P - S$ separation with source location at 0m, showing: (a) Horizontal component of normal stress ( $\tau_{xx}$ ); (b) Divergence ( $P - P$ ); and (c) Curl ( $P - S$ ). . . . . 71
5.5	Inversion scheme that uses migration to calculate the reflection coefficients, $R_{PP}$ and $R_{PS}$ directly from seismic data. . . . . 73

## CHAPTER I

### WHY SOLVING FOR POISSON'S RATIO: ACTUAL VALUE VERSUS CONTRAST

In 1984, W. J. Ostrander proposed a new theory in seismic interpretation, better known as amplitude variation with offset (AVO). Ostrander's theory is based on the variation of the reflection coefficients with offset. Ostrander observed that the manner in which a reflection coefficient varies mostly depends on the contrasts of elastic parameters between the two media, namely the contrast of Poisson's ratio. This remark is particularly important because of the major role that Poisson's ratio plays as a lithology-identification factor. Upon these premises, we propose a new direct approach to the problem of identifying subsurface materials based on the specific values of Poisson's ratio extracted from an AVO analysis that combines  $P - P$  and  $P - S$  data.

Originally, the majority of the work done in AVO was focused on compressional  $P - P$  reflection (Ensley, 1984). Ocean bottom seismology (OBS) has allowed extraction and exploitation of converted shear-wave data ( $P - S$ ). Studies have shown  $P - S$  imaging to be preferable to conventional  $P - P$  imaging in certain circumstances, such as a small acoustic impedance contrast (Engelmark, 2000). This project, therefore, combines both  $P - P$  and  $P - S$  data for a better insight in identifying subsurface materials.

Most of the existing combined AVO work only solves for contrast of elastic prop-

---

This thesis follows the style and format of Geophysics.

erties within an interval. In this thesis, I propose a method that, by combining  $P - P$  and  $P - S$  reflection data, will provide a direct way of lithology identification. In particular, the objective of this thesis is to prove the feasibility of a scheme that accurately estimates specific values for the  $V_P/V_S$  ratio and Poisson's ratio for each lithology in a given geological model.

Our analysis will be based on Zoeppritz' solution for the  $P - P$  and  $P - S$  reflection coefficients,  $R_{PP}$  and  $R_{PS}$ , with a slight modification. Instead of  $R_{PS}$ , I used the normalized  $P - S$  reflection coefficient defined in terms of the incident angle,  $\theta$ , as follows:

$$R'_{PS} = \frac{R_{PS}}{\sin \theta} \text{ for } \theta > 0 . \quad (1.1)$$

Using a linear approximation for the reflection coefficients at angles of less than 35 degrees, I will develop a nonlinear inversion scheme that allows us to estimate the contrasts of  $P$ - and  $S$ -wave velocities, the contrast of density, and the average  $V_P/V_S$  ratio, for a given half-space model (2-layer case). With this information, we should be able to solve for the  $V_P/V_S$  ratio of each layer in the model ( $[V_P/V_S]_k$ , with  $k = 1$ : top layer, and  $k = 2$ : bottom layer). And consequently, we can estimate the specific Poisson's ratio for the same formations, enabling lithology discrimination.

In summary, AVO has formerly aimed to estimate the contrast of elastic parameters (i.e.,  $\Delta V_P/V_P$ ,  $\Delta V_S/V_S$ , and  $\Delta \rho/\rho$ ) that describe interfaces only, not lithologies. This thesis will review the theoretical basis for a method of lithology identification that not only finds the elastic parameter contrasts, but it also estimates the average  $V_P/V_S$  ratio, and uses all of this information to calculate the actual value of Poisson's ratio of each lithology in the model.



## 1.1 Problem Description

Elastic parameters derived from seismic data are valuable information in reservoir characterization since they can be directly related to lithology and to the fluid content of a reservoir (Landro and Veire, 2001). However, very limited knowledge exists on the elastic parameters of subsurface materials. This complication sets the target problem of this project: lithology identification.

In addition to the lack of information about elastic properties, we may add difficulty regarding the availability and processing of  $P - S$  data as a hindrance to lithology identification. According to Garotta et al. (2002), because shear information cannot be easily integrated into the normal interpretation workflow, it is seldom used. However, if the right tools allow effortless extraction of the full shear-wave information, the added benefits far outweigh the acquisition cost. In this thesis I would like to present one such tool and show that combined interpretation of  $P - P$  and  $P - S$  data provides reliable estimates of elastic rock properties.

## 1.2 Previous Work

Since Ostrander (1984) proposed the new theory of seismic interpretation two decades ago, known as amplitude variation with offset (AVO), a significant amount of work has been done in the area. According to Castagna (1993), the benefits of this theory lie in the theoretical relationship among the reflection coefficient, the incident angle, and the variation in compressional-wave velocity ( $V_P$ ), shear-wave velocity ( $V_S$ ), and density ( $\rho$ ) across an interface. Originally, though, as Ensley (1984) points out, most of the work in AVO analysis was focused on compressional-wave reflection. The use of "bright spots", or  $P$ -wave impedance contrasts, became very popular.

And the use of shear-wave data for hydrocarbon detection was, at the time, limited to qualitative analyses.

Subsequent improvements in the extraction and quality  $P - S$  data have led to the development of more quantitative methods. Ocean bottom seismic, OBS, has been around for more than 30 years but has struggled to earn popularity. As we have already mentioned, the better tools we develop for shear-wave information extraction, the more acceptance multicomponent seismic gains, and the more benefits in exploration seismology are obtained.

Shear waves differ from compressional waves in that shear waves are insensitive to fluids, slower than compressional waves, and polarized (Garotta et al., 2002). These differences suggest that combination of  $P - P$  and  $P - S$  information embraces potential for (1) fluid and lithology identification, (2) imaging structure through gas clouds, (3) increased resolution, (4) imaging low-acoustic impedance reservoirs, and (5) fracture detection by analysis of shear-wave splitting. Aiming to these expected benefits of combined  $P - P$  and  $P - S$  analyses, extensive work has been done in the area [e.g., Jin's (1999) work on reservoir characterization, Landro and Veire's (2001) least squares inversion, Garotta et al.'s (2002) reconciliation of arrival times for elastic parameters, and Ensley's (1984) comparison of  $P$ - and  $S$ -wave data].

### 1.3 Methodology

Most of the combined classical AVO work solves only for contrast of elastic properties within an interval. Here we would like to propose a method that, by combining  $P - P$  and  $P - S$  reflection data, will lead to the estimation of specific values of Poisson's ratio for every rock formation within a geological interval and, in turn, to the identification of such a formation.

To develop this method, we will look at the linear behavior of both reflection coefficients,  $R_{PP}$  and  $R'_{PS}$ , for angles smaller than 35 degrees. This problem is a forward-modeling process that entails the creation and study of several theoretical half-space models. It will be necessary to graph the reflection coefficients for each model as a function of the squared sine of the incident angle. On top of this plot, a linear approximation should be calculated for the small angles. Using a linear approximation similar to that of Aki and Richards, 1980, we will develop a non-linear inversion scheme, which in turn will allow us to estimate the contrasts of  $P$ - and  $S$ -wave velocities, the contrast of density, and the average  $V_P/V_S$  ratio. Separately, we should derive the equations that describe the actual value of the  $V_P/V_S$  ratio for each lithology in the model ( $[V_P/V_S]_1$  for the top layer, and  $[V_P/V_S]_2$  for the bottom layer) as a function of the seismic velocity contrasts and of the average  $V_P/V_S$  ratio. Consequently, we can estimate the specific Poisson's ratio of each of these formations, enabling their lithology identification. These derivations go beyond our earlier work (Carcuz, 2001), where we found only elastic contrasts and the average  $V_P/V_S$  ratio.

Since we have developed our own models, we can compare our final results with the theoretical values to prove the validity of our algorithm. In addition, least-square cost function plots can be generated to look at the margin of error as well as to validate the uniqueness and precision of the solution. Once this inversion algorithm is proven to be effective for flat interfaces, we can take it a step further by generalizing all of the governing equations for dipping interfaces. Finally, using finite-difference code, we will generate synthetic models based on the previous theoretical models to see how this method behaves in front of synthetic seismic data. This process will include recovery of reflection coefficients from seismic data using an algorithm similar to that used by Ikelle et al. (1986 and 1988).

## 1.4 Assumptions

This algorithm is valid if certain assumptions are made. To reach our objective, we will assume reliable  $P - P$  and  $P - S$  reflection data. Compressional waves are sensitive to the type of pore fluid within rocks, but shear waves may not even be affected by changes in fluid type. This observation suggests that a comparison of compressional- and shear-wave seismic data may allow an interpreter to discriminate lithology anomalies (Ensley, 1984). On this basis, we will also assume that a comparison of the similarities and differences between  $P - P$  and  $P - S$  data will improve our processing.

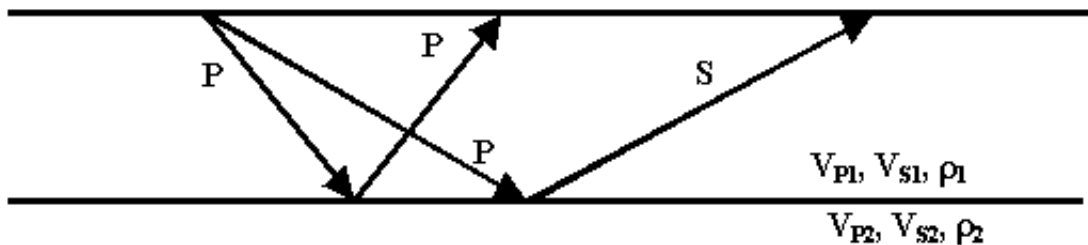


Fig. 1.1. Problem to analyze: A half-space model where the elastic parameters of each media are  $V_{P1}$ ,  $V_{S1}$ ,  $\rho_1$ ,  $V_{P2}$ ,  $V_{S2}$ , and  $\rho_2$ , and two seismic events take place: reflection of  $P$ -wave and its conversion into  $S$ -wave.

Let us consider Figure 1.1. Regarding the physics and geometry of the problem, we will initially assume that all models studied are simple heterogeneous isotropic half-space models. Assume a flat interface, which we will later generalize to a dipping interface. Let us also consider an incident compressional plane wave impinging upon this interface. Only two seismic events are considered:  $P$ -wave reflection ( $P - P$ ), and its respective conversion to  $S$ -wave ( $P - S$ ). The plane-wave assumption is valid at source-to-receiver distances, which are much longer than the wavelength of the

incident wave and is generally acceptable for precritical reflection data at exploration depths and frequencies (Castagna, 1993).

## 1.5 Novelty and Importance

AVO is currently a widely accepted theory in the area of seismic interpretation. It provides a good insight about the subsurface while maintaining low costs of execution. Nonetheless, no work in this area has found a solution to the problem of accurate rock-formation discrimination based on seismic surveying. Most of the combined  $P - P$  and  $P - S$  AVO analyses currently done in the oil industry solve only for the average or contrast of elastic properties within a geological interval. Although according to Ensley (1984) high acoustic impedance contrasts (i.e., bright spots) seem to be a reliable indicator for hydrocarbon detection, Ross and Kinman (1995) present evidence that shows this is not always the case. To the best of my knowledge, no AVO analysis has yet found a solution to the estimation of the specific elastic properties of each material in the subsurface. The novelty of this thesis is that it proposes a scheme that, by combining  $P - P$  and  $P - S$  reflection data, will provide the theoretical foundation for a direct method of lithology identification by estimating the specific values of Poisson's ratio for each different lithology in a geological model. In fact, the compilation of one complete algorithm that combines such processing steps as geometrical-spreading correction, migration, and AVO analysis, is another novelty of our work, which leads to finding the specific values of Poisson's ratio of each rock formation directly from the seismic data.

The value of this research lies in the estimation of Poisson's ratio as a lithology identifier. There exist several methods of describing isotropic elastic rock formations using three independent parameters:

- Lamé parameters ( $\lambda$  and  $\mu$ ) and density ( $\rho$ )
- $P$ -wave velocity ( $V_P$ ),  $S$ -wave velocity ( $V_S$ ), and density ( $\rho$ )
- $P$ -wave impedance ( $Z_P$ ),  $S$ -wave impedance ( $Z_S$ ), and density ( $\rho$ )
- Poisson's ratio ( $\sigma$ ),  $P$ -wave velocity ( $V_P$ ), and density ( $\rho$ )

Difficulty still exists to determine accurate seismic velocities using AVO, which represents a challenge for further research. We will therefore use Poisson's ratio, as defined by equation (1.2), for lithology discrimination.

$$\sigma = \frac{\frac{1}{2} \left( \frac{V_P}{V_S} \right)^2 - 1}{\left( \frac{V_P}{V_S} \right)^2 - 1}. \quad (1.2)$$

Table 1.1. Poisson's ratio for common lithologies.

Lithology	Poisson's Ratio
Consolidated shale	0.25 – 0.35
Consolidated sandstone	0.15 – 0.25
Unconsolidated shale	0.35 – 0.45
Unconsolidated sandstone	0.30 – 0.35
High-porosity sandstone	0.35 – 0.40
Low-porosity sandstone	0.15 – 0.25
Gas-charged sandstone	0.10 – 0.20
Oil-saturated sandstone	0.28 – 0.32
Salt	0.25 – 0.30
Dolomite	0.25 – 0.30
Limestone	0.25 - 0.35
Coal	0.35 - 0.45

Poisson's ratio alone is not sufficient to identify a given rock formation. Yet it narrows the choices. Table 1.1 contains examples of experimental measurements of Poisson's ratio for common materials. Pilkington (1988) attributes the variations of elastic properties (i.e., Poisson's ratio) to geological conditions such as pressure and temperature, which are in turn dependent on depth. Therefore, with a little information about the geometry of the subsurface, which can also be extracted from seismic data, Poisson's ratio may provide the missing link to lithology identification. Furthermore, in his overpressure detection study, Prasad (2002) found a direct relation between Poisson's ratio and load-bearing sediments undergoing suspension. He showed that as a load-bearing sediment approaches a state of suspension, Poisson's ratio increases exponentially while it decreases in the presence of gas. In conclusion, we can safely say that estimation of Poisson's ratio provides powerful information for lithology description and discrimination.

## 1.6 Scope of This Thesis

Throughout this thesis, I will thoroughly describe a method that combines  $P-P$  and  $P-S$  reflection data to estimate the actual value of Poisson's ratio for each rock formation, and therefore better approach the problem of identifying subsurface materials. I intend to show the theoretical aspects behind this method and to provide practical examples using synthetic seismic data. To reach this objective, I have divided the problem into six chapters, which I briefly review below.

### 1.6.1 AVO Analysis Combining $P - P$ and $P - S$ Data: A Nonlinear Inversion for Poisson's Ratio

Chapter II describes in detail the theoretical foundations used to pursue our objective, as outlined above. It departs from the assumption that the similarities and differences between reflection coefficients may allow an interpreter to discriminate lithology anomalies (Ensley, 1984). It also points out the need for normalization of the  $P - S$  reflection coefficient. In this chapter we look at the linear behavior of  $R_{PP}$  and  $R'_{PS}$  at near offsets and develop several theoretical models to test our results. Using a linear approximation similar to that of Aki and Richards, 1980, we set up a nonlinear inversion scheme, which allows us to estimate the contrasts of  $P$ - and  $S$ -wave velocities, the contrast of density, and the average  $V_P/V_S$  ratio. Finally, we derive the equations for the  $V_P/V_S$  ratio of each formation above and below the interface, and for Poisson's ratio ( $\sigma_k$ ). These equations are applied to the testing models to check for accuracy of our method.

### 1.6.2 An Application to Finite-Difference Simulations

Using finite difference code, we generate synthetic models based on the theoretical models used in Chapter II to see how this method will respond to synthetic seismic data. In this third chapter, we describe a flow chart for the inversion scheme. According to this chart, the input to the inversion scheme will be the reflection coefficients extracted from the seismic data. We compare these reflection coefficients to those expected from the use of Zoeppritz' equations. Once they are validated, we process these coefficients following the algorithm described in the previous chapter and discuss the results.



### 1.6.3 Analysis and Generalization for Dipping Interfaces

In reality, seismic reflectors are seldom horizontally flat. To comply with this constraint, we generalize the governing equations for this algorithm to dipping interfaces, after we have shown its effectiveness for flat interfaces. Our experience finds that the amplitude variation with offset of  $P - P$  and  $P - S$  for a dipping interface can be cast into intercepts and gradients. However, these intercepts and gradients depend on the angle of the dipping interface. We further generalize our analysis by including a migration step that allows us to find the dipping angle.

### 1.6.4 An Integrated Approach to Migration and AVO Inversion

Chapter III does not explain in much detail how the reflection coefficients are extracted from seismic data. Recovery of reflection coefficients from seismic data requires several considerations, such as the effects of geometrical spreading, normal move out, and calibration. Ikelle et al. (1986, 1988) developed an algorithm that takes care of this problem. In Chapter V, we describe the theory behind this algorithm, we develop more-complicated synthetic seismic data, and we review how the algorithm will be applied to the data.

This will lead us into drawing conclusions, which will summarize the theory, process, and results of combining  $P - P$  and  $P - S$  reflection data for an accurate quantitative method of lithology identification based upon an estimation of Poisson's ratio for each rock formation present in a seismic experiment.

## CHAPTER II

### AVO ANALYSIS COMBINING $P - P$ AND $P - S$ DATA: A NONLINEAR INVERSION FOR POISSON'S RATIO

The problem of identifying subsurface materials represents a current challenge in geophysical research. Landro and Veire (2001) explain that elastic parameters derived from seismic data contain valuable information in reservoir characterization. Therefore, my objective in this chapter will be to estimate such elastic parameters (i.e.,  $\Delta V_P/V_P$ ,  $\Delta V_S/V_S$ ,  $\Delta\rho/\rho$ , and  $V_P/V_S$ ) for half-space models, and to use these parameters to deduce Poisson's ratio for each half-space, by jointly analyzing  $P - P$  and  $P - S$  data. Identification of specific values of Poisson's ratio for individual rock formations should bring valuable information to the problem of identifying subsurface materials.

#### 2.1 Definition of Models

To focus our discussion, let us set up a forward problem by considering four simple isotropic half-space (two-layer) models: an unconsolidated shale/sand model, a shale/salt model, a shale/limestone (gas) model, and a shale/salt model. Two seismic events are taking place: the reflection of an incident compressional wave ( $P - P$ ) and its conversion into a shear wave ( $P - S$ ), as shown in Figure 1.1. Table 2.1 contains the elastic parameters of each of these models. These parameters are similar to those used by Engelmark (2000). Figure 2.1 shows the  $P - P$  and  $P - S$  reflection coefficients of each of the four models as functions of  $\sin^2 \theta$ , where  $\theta$  is the incident angle.

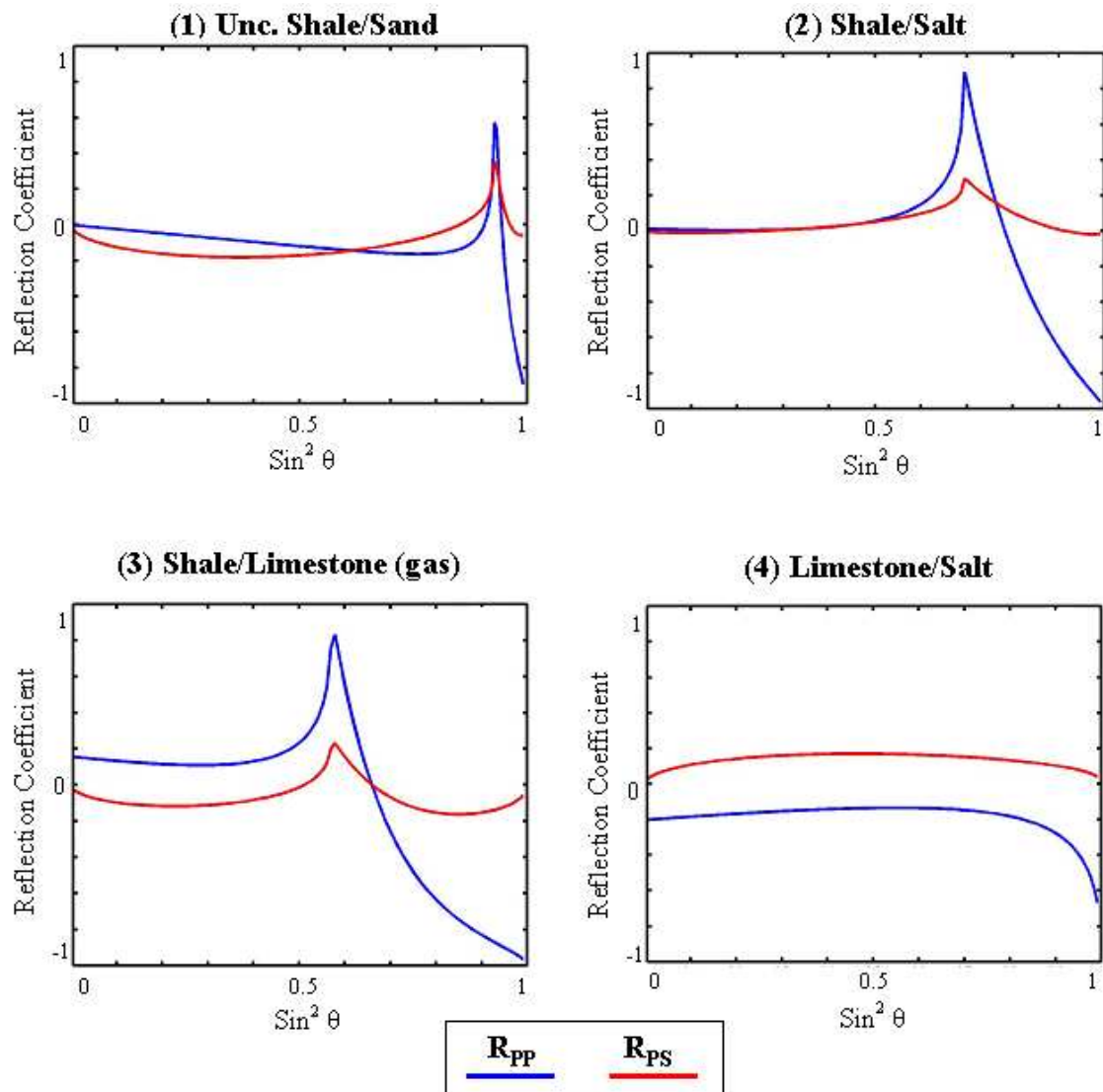


Fig. 2.1.  $P - P$  (blue) and  $P - S$  (red) reflection coefficients for the four models described in Table 2.1. There is not an obvious relationship between  $R_{PP}$  and  $R_{PS}$ , which we attribute to the nonlinear behavior of  $R_{PS}$ .

Table 2.1. Elastic Parameters for four differing half-space models: unconsolidated shale/sand, shale/salt, gas shale/limestone, and limestone/salt [ $V_P$  :  $P$ -wave velocity;  $V_S$  :  $S$ -wave velocity; and  $\rho$  : density].

Model	Rock Type	Material	$V_P(Km/s)$	$V_S(Km/s)$	$\rho(g/cc)$
1	Shale/Sand (unconsolidated)	Shale	2.057	0.4895	2.16
		Sand	2.134	0.9693	2.08
2	Shale/Salt	Shale	3.811	2.263	2.40
		Salt	4.573	2.729	2.05
3	Shale/Limestone (gas)	Shale	3.811	2.263	2.40
		Limestone	5.043	2.957	2.49
4	Limestone/Salt	Limestone	5.335	2.957	2.65
		Salt	4.573	2.729	2.05

### 2.1.1 Normalization of $R_{PS}$

We have calculated the reflection coefficients directly from the elastic parameters in Table 2.1 based on Zoeppritz' solution for  $R_{PP}$  and  $R_{PS}$ . Notice that variations of  $R_{PP}$  and of  $R_{PS}$  with  $\theta$  are quite different. Instead of  $R_{PS}$ , let us consider  $R'_{PS}$ , as defined by equation (2.1). By normalizing  $R_{PS}$ , we enhance the existing similarities between  $R_{PP}$  and  $R'_{PS}$  (i.e., linearity at small incident angles) as well as their differences. Figure 2.2 shows  $R_{PP}$  and  $R'_{PS}$  for the same models used in Figure 2.1;

$$R'_{PS} = \frac{R_{PS}}{\sin \theta} \text{ for } \theta > 0 . \quad (2.1)$$

### 2.1.2 Similarities and Differences Between $R_{PP}$ and $R'_{PS}$

We can see that the variations with the incident angle of  $R_{PP}$  and the normalized converted  $S$ -wave reflection coefficient  $R'_{PS}$  are quite similar. In a way, they seem to

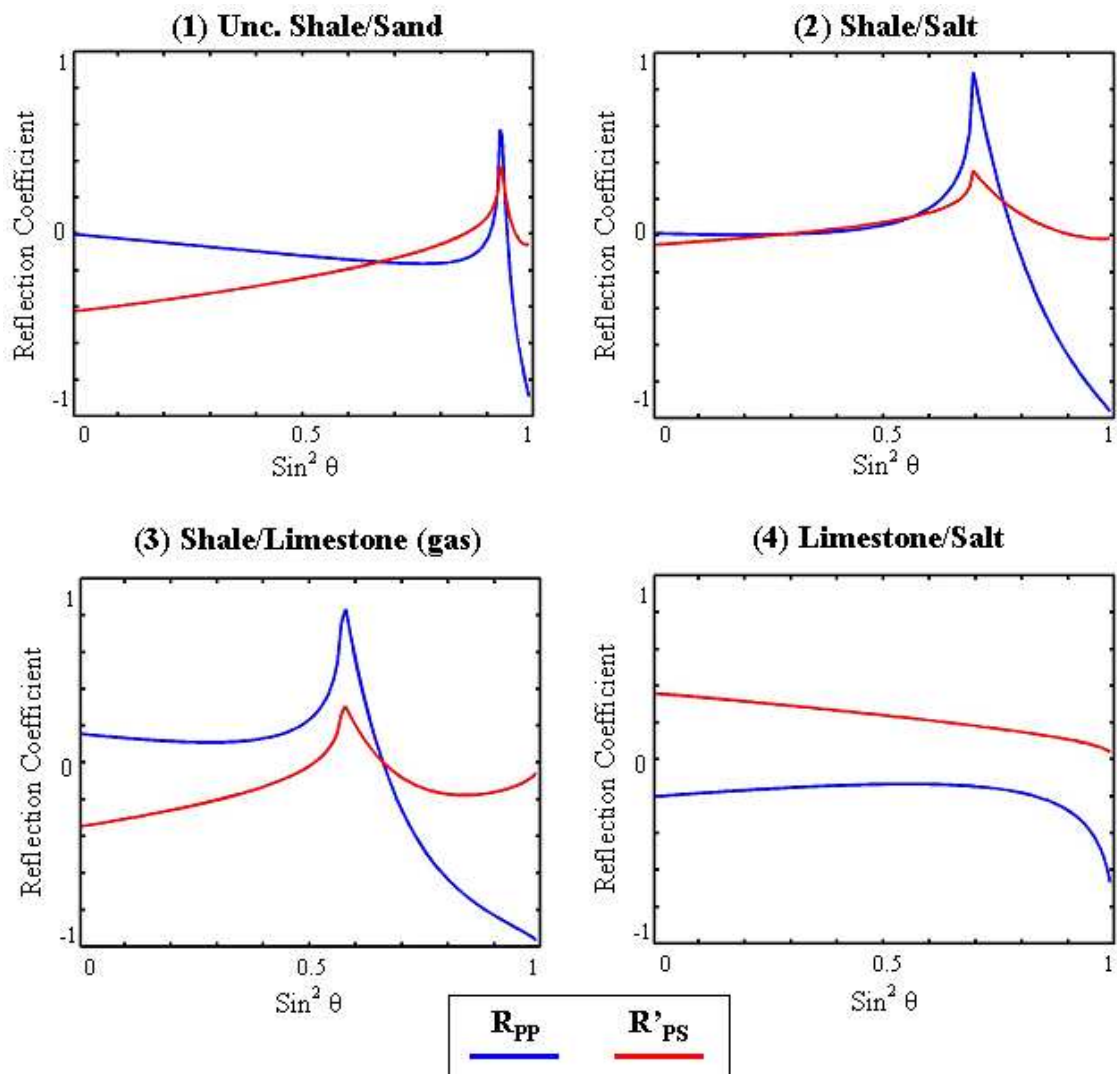


Fig. 2.2.  $P - P$  (blue) and normalized  $P - S$  (red) reflection coefficients for the four models described in Table 2.1. Now  $R'_{PS}$  does behave similarly to  $R_{PP}$ . At small angles, they run linearly with opposite gradient, they peak at the critical angle, and they drop down abruptly.  $R'_{PS}$  is not defined at zero; thus this figure begins at an angle slightly greater than zero.

track each other and behave similarly, as shown by Figure 2.2. Both of them show a linear trend at small angles, eventually meet at a point of interception, blow up, peak at the same place (the critical angle), and from there, abruptly drop down. Their rise at the critical angle is due to the lack of transmitted energy at that point. Model four is an exception to this phenomenon due to its negative impedance contrasts.

There are also differences between  $R_{PP}$  and  $R'_{PS}$ . Among the differences we can mention the peak heights at the critical angle. More important, we can observe the opposite arithmetic sign of the linear gradient at small incident angles (i.e.,  $\theta < 35^\circ$ ) due to the conservation of energy;  $R_{PP}$  decreases when  $R'_{PS}$  increases and vice versa, as illustrated in Figure 2.2. In fact, our experience in analyzing  $R_{PP}$  and  $R'_{PS}$  for multiple contrasts between several rock formations, including all of the models in Table 2.1, suggests that the gradient of  $R_{PP}$ , at small angles of incidence, is most of the time opposite to the gradient of  $R'_{PS}$ ; in other words, when the gradient of  $R_{PP}$  is positive, that of  $R'_{PS}$  is negative, and vice versa. Which gradient is positive and which is negative depends on which one has the greater intercept, which in turn relies on the acoustic impedance on the two media. As it is known, the intercept is positive if the impedance of the underlying layer is greater than that of the upper layer, and vice versa. Figure 2.3 shows different trends for the gradient of  $R_{PP}$  and  $R'_{PS}$ . As we mentioned, these gradients are expected to be opposite and run towards each other to comply with the law of conservation of energy. Figure 2.3a shows one such case. Figures 2.3b, 2.3c, and 2.3d show unrealistic cases, as the gradients are not expected to have the same arithmetic sign, or to be opposite and away from each other at the same time.

The similarities and differences described here can be used to find the  $P - S$  reflection in seismic data, which can be associated with a given  $P - P$  reflection.

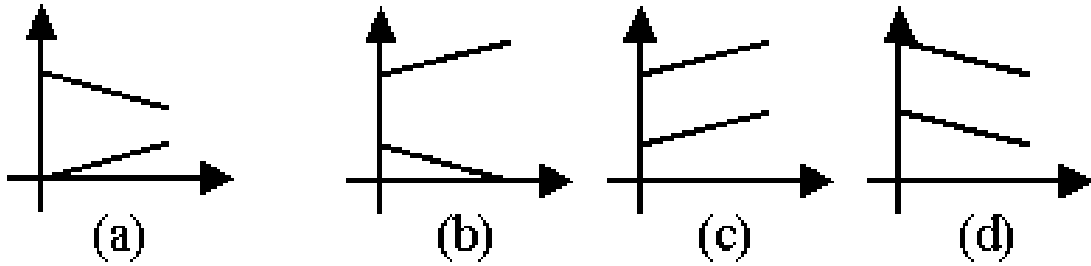


Fig. 2.3. Different trends of reflection coefficient gradients: (a) opposite gradient towards each other. (b) opposite gradient away from each other. (c) both positive gradients. (d) both negative gradients. Only (a) is considered realistic.

## 2.2 Small-Angle Linear Approximation

### 2.2.1 Linear Approximation Equations

Let us look in more detail at the linear behavior of the reflection coefficients  $R_{PP}$  and  $R'_{PS}$  at small angles. We have already mentioned their opposite gradient. This feature contains valuable information about lithology.

At small angles,  $R_{PP}$  and  $R'_{PS}$  can be approximated by

$$R_{PP} = A_{PP} + B_{PP} \sin^2 \theta , \quad (2.2)$$

$$\text{and } R'_{PS} = A_{PS} + B_{PS} \sin^2 \theta , \quad (2.3)$$

where

$$A_{PP} = \frac{1}{2} \left( \frac{\Delta \rho}{\rho} + \frac{\Delta V_P}{V_P} \right) , \quad (2.4)$$

$$B_{PP} = \frac{1}{2} \frac{\Delta V_P}{V_P} - 2 \frac{V_S^2}{V_P^2} \left( \frac{\Delta \rho}{\rho} + 2 \frac{\Delta V_S}{V_S} \right) , \quad (2.5)$$

$$A_{PS} = -\frac{1}{2} \frac{\Delta \rho}{\rho} - \frac{V_S}{V_P} \left( \frac{\Delta \rho}{\rho} + 2 \frac{\Delta V_S}{V_S} \right) , \quad (2.6)$$

$$B_{PS} = -\frac{1}{2} \frac{V_S^2}{V_P^2} \left[ \frac{\Delta\rho}{\rho} - \left( 1 + \frac{V_P}{V_S} \right) \left( \frac{\Delta\rho}{\rho} + 2 \frac{\Delta V_S}{V_S} \right) \right]. \quad (2.7)$$

$A_{PP}$  and  $A_{PS}$  are intercepts, and  $B_{PP}$  and  $B_{PS}$  are gradients. These approximations are similar to those of Aki and Richards (1980). There exist several linear approximations to the Zoeppritz' equations (e.g., Aki and Richards, 1980, Bortfeld, 1961, Shuey, 1985, Fatti et al., 1994, Smith and Gidlow, 1987); but we have chosen Aki and Richards's because it has the advantage that it simplifies the inversion procedure by changing the independent variables to  $\Delta V_P/V_P$ ,  $\Delta V_S/V_S$ ,  $\Delta\rho/\rho$ , and  $V_P/V_S$ : four independent parameters, which we will solve for.

### 2.2.2 Validation of Linear Approximations

We have validated these approximations using the models described in Table 2.1. Figure 2.4 shows the linear behavior of  $R_{PP}$  and  $R'_{PS}$  for the four models when the incident angle,  $\theta$ , is less than 35 degrees. This figure also displays the linear approximations obtained from equations (2.2-2.7). Table 2.2 shows the numerical values of the intercepts ( $A_{PP}$  and  $A_{PS}$ ) and gradients ( $B_{PP}$  and  $B_{PS}$ ) for each model, as extracted from their linear approximations. These values will become useful when we set up the inversion scheme, as they will represent the known values of the system.

Table 2.2. Numerical values of the intercepts and gradients [ $A_{PP}$ :  $R_{PP}$  intercept;  $B_{PP}$ :  $R_{PP}$  gradient;  $A_{PS}$ :  $R'_{PS}$  intercept; and  $B_{PS}$ :  $R'_{PS}$  gradient].

Model	Rock Type	$A_{PP}$	$B_{PP}$	$A_{PS}$	$B_{PS}$
1	Unc. Shale/Sand	-0.0005	-0.2913	-0.4259	0.3010
2	Shale/Salt	0.0123	-0.0623	-0.0500	0.1166
3	Gas Shale/Limestone	0.1571	-0.2561	-0.3536	0.2632
4	Limestone/Salt	-0.2026	0.1969	0.3662	-0.1667



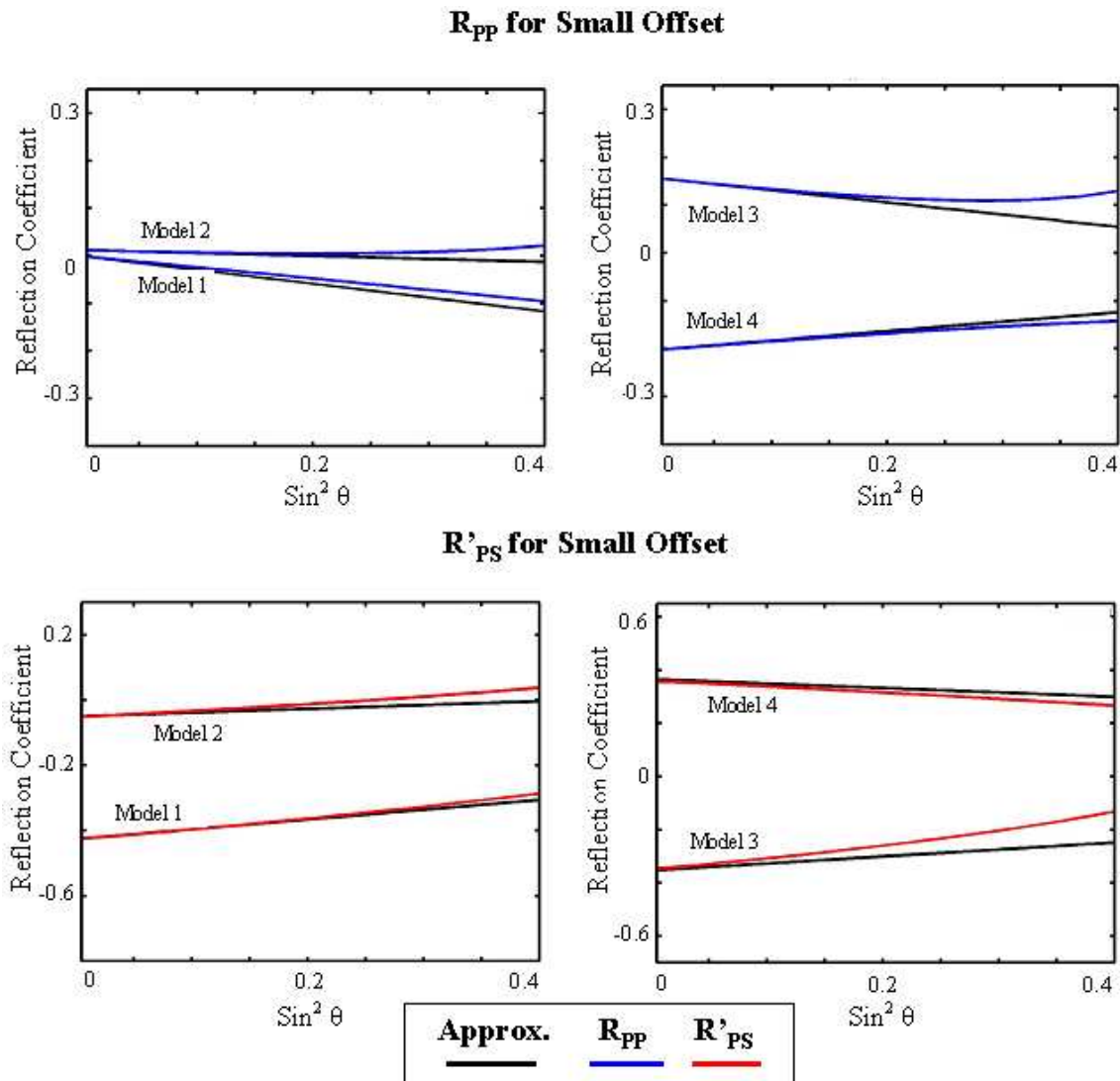


Fig. 2.4. Linear approximation (black) for the  $P - P$  reflection coefficient (blue) and the normalized  $P - S$  reflection coefficient (red), obtained from equations (2.2-2.7) for the four models described in Table 2.1. Because  $R'_{PS}$  is not defined at zero, this figure begins at an angle slightly greater than zero.

### 2.2.3 Discussion

The linear approximations displayed in Figure 2.4 (black) precisely follow the reflective trend up to about 30 degrees. The misfit of the linear approximations as they approach 35 degrees may slightly increase the uncertainty when applying the inversion scheme; however, we can safely expect to have a relatively small uncertainty. Moreover, we can notice that the values of the intercepts of  $R_{PP}$  for the unconsolidated shale/sand model and the shale/salt model (models 1 and 2) are almost identical (or at least within the margin of error in most real data cases), whereas the values of the intercepts of  $R'_{PS}$  are quite distinct. This result is not surprising since the acoustic impedance contrast for these two models is almost null. This difference shows that the variations of  $R'_{PS}$  can be useful in discriminating between lithologies when the variations of  $R_{PP}$  are small.

As we noticed earlier, when looking at the normalized reflection coefficients based on Zoeppritz' equations (Figure 2.2), we can see from Figure 2.4 that the gradients  $R_{PP}$  and  $R'_{PS}$  for these four models also have opposite sign. In general the gradients  $R_{PP}$  and  $R'_{PS}$  can be either positive or negative. However, our experience suggests that they are always opposite.

## 2.3 Nonlinear Inversion for Elastic Contrasts and $V_P/V_S$

### 2.3.1 Objective

Equations (2.4-2.7) form a system of four independent equations with four unknown elastic parameters (e.g.,  $\Delta V_P/V_P$ ,  $\Delta V_S/V_S$ ,  $\Delta\rho/\rho$ , and  $V_P/V_S$ ). Our next task is to estimate these elastic parameters from a given set of  $P - P$  and  $P - S$  AVO intercepts and gradients (i.e.,  $A_{PP}$ ,  $A_{PS}$ ,  $B_{PP}$ , and  $B_{PS}$ , shown in Table 2.2) by solv-

ing system of equations (2.4-2.7). The solution to this system is important in seismic exploration and production because it increases the number of parameters that we can recover from seismic data, which in turn can be used to improve the identification and discrimination of the various subsurface lithologies.

### 2.3.2 Inversion

Up to this point we have developed a forward model of the reflection coefficients,  $R_{PP}$  and  $R'_{PS}$ , based on the elastic parameters of the materials. Let us now look at the inverse problem to solve for these parameters. The system of equations (2.4-2.7) is nonlinear. This nonlinearity is brought in by the  $V_P/V_S$  ratio with powers of -1 and -2. We can use an iterative scheme to solve the system. Equations (2.4-2.7) can be rewritten as

$$A_{PP} = \frac{1}{2}(x_3 + x_1) , \quad (2.8)$$

$$B_{PP} = \frac{1}{2}x_1 - 2x_4^2(x_3 + 2x_2) , \quad (2.9)$$

$$A_{PS} = -\frac{1}{2}x_3 - x_4(x_3 + 2x_2) , \quad (2.10)$$

$$B_{PS} = \frac{1}{2}x_4^2 \left( 2x_2 + \frac{x_3}{x_4} + 2\frac{x_2}{x_4} \right) , \quad (2.11)$$

where

$$x_1 = \frac{\Delta V_P}{V_P} , \quad x_2 = \frac{\Delta V_S}{V_S} , \quad x_3 = \frac{\Delta \rho}{\rho} , \quad \text{and} \quad x_4 = \frac{V_S}{V_P} . \quad (2.12)$$

To solve the problem of nonlinearity, we can substitute each variable  $x_i$  (for  $i = 1..4$ ) in (2.8-2.11) by  $x_{oi} + x'_i$ , where  $x_{oi}$  will be an initial guess and  $x'_i$  a small value

(unknown) that will represent the new variable to the system. This substitution yields the following system, which we can solve iteratively:

$$\begin{aligned} & B_{PP} - A_{PP} + \frac{1}{2}x_{o3} - 2x_{o3}x_{o4}^2 + 4x_{o2}x_{o4}^2 \\ &= -4(x_{o3}x_{o4} + 2x_{o2}x_{o4})x_4' - \left(\frac{1}{2} + 2x_{o4}^2\right)x_3' - 4x_{o4}^2x_2' \end{aligned} \quad (2.13)$$

$$\begin{aligned} & A_{PS} + \frac{1}{2}x_{o3} + x_{o3}x_{o4} + 2x_{o2}x_{o4} \\ &= -(2x_{o2} + x_{o3})x_4' - \left(\frac{1}{2} + 2x_{o4}\right)x_3' - 2x_{o4}x_2' \end{aligned} \quad (2.14)$$

$$\begin{aligned} & -2B_{PS} + 2x_{o2}x_{o4}^2 + x_{o3}x_{o4} + 2x_{o2}x_{o4} \\ &= -(x_{o3} + 2x_{o2} + 4x_{o2}x_{o4})x_4' - x_{o4}x_3' - 2x_{o4}(x_{o4} + 1)x_2' \end{aligned} \quad (2.15)$$

### 2.3.3 Results

Our initial guess ( $x_{oi}$ ) for  $\Delta V_P/V_P$ ,  $\Delta V_S/V_S$  and  $\Delta\rho/\rho$  was 0.0001, and for the  $V_P/V_S$  ratio it was 1.5. These initial values were chosen based on our previous knowledge about these parameters. Because all of the contrasts are normalized values, they are expected to fall between zero and one. And in regard to the  $V_P/V_S$ , 1.5 represents one of the smallest realistic values that it can have.

Fortunately, the solution to this nonlinear system converges rapidly to a unique solution, even if the starting model has a negative Poisson's Ratio (i.e., unrealistic  $V_P/V_S$  ratios for earth rock formations.) Table 2.3 shows the estimated and actual values of  $\Delta V_P/V_P$ ,  $\Delta V_S/V_S$ ,  $\Delta\rho/\rho$  and  $V_P/V_S$  for the models of material contrast considered in this chapter. When compared to the actual values, our estimated values are quite accurate, with less than a 1 percent error, which we attribute to misfits in the linear approximations as incident angles approach 35 degrees.

Table 2.3. Estimated and actual values of  $\Delta V_P/V_P$ ,  $\Delta V_S/V_S$ ,  $\Delta\rho/\rho$ , and  $V_P/V_S$ . The less-than-1-percent error of approximation between estimated and actual values shows the accuracy of the inversion process.

Model	Rock Type	Value	$\Delta V_P/V_P$	$\Delta V_S/V_S$	$\Delta\rho/\rho$	$V_P/V_S$
1	Shale/Sand (unconsolidated)	Estimated	0.0343	0.6554	-0.0352	2.8760
		Actual	0.0367	0.6578	-0.0377	2.8729
2	Shale/Salt	Estimated	0.1551	0.1602	-0.1305	1.6482
		Actual	0.1818	0.1867	-0.1573	1.6795
3	Shale/Limestone (gas)	Estimated	0.2834	0.2721	0.0308	1.7003
		Actual	0.2783	0.2659	0.0368	1.6962
4	Limestone/Salt	Estimated	-0.1876	-0.1191	-0.2176	1.7709
		Actual	-0.1670	-0.1375	-0.1998	1.7717

### 2.3.4 Discussion

Figure 2.5 shows the variation of the least-square cost function,  $L$ , defined by equation (2.16), as the  $V_P/V_S$  ratio is changed. We chose to display the variations of this function with the  $V_P/V_S$  ratio because the nonlinearity of the system of equations (2.8-2.11) is caused by the introduction of  $V_P/V_S$  as one of the unknowns. As we can see in Figure 2.5, a scan over the values of  $V_P/V_S$ , including unrealistic ones, not only confirms the uniqueness of our solution, but it proves the accuracy of the results obtained from the iterative scheme. In fact, the results in Figure 2.5, based on each of the four models, show that the system has a unique solution for any realistic and unrealistic values. Actually, our experience with other models not included in this chapter, yields variations of the least-square cost function with values of the  $V_P/V_S$  ratio similar to those in Figure 2.5.

$$L = \frac{\| [B_{PS}]^{OBS} - [B_{PS}]^{EST} \|^2}{\| [B_{PS}]^{OBS} \|^2}, \quad (2.16)$$

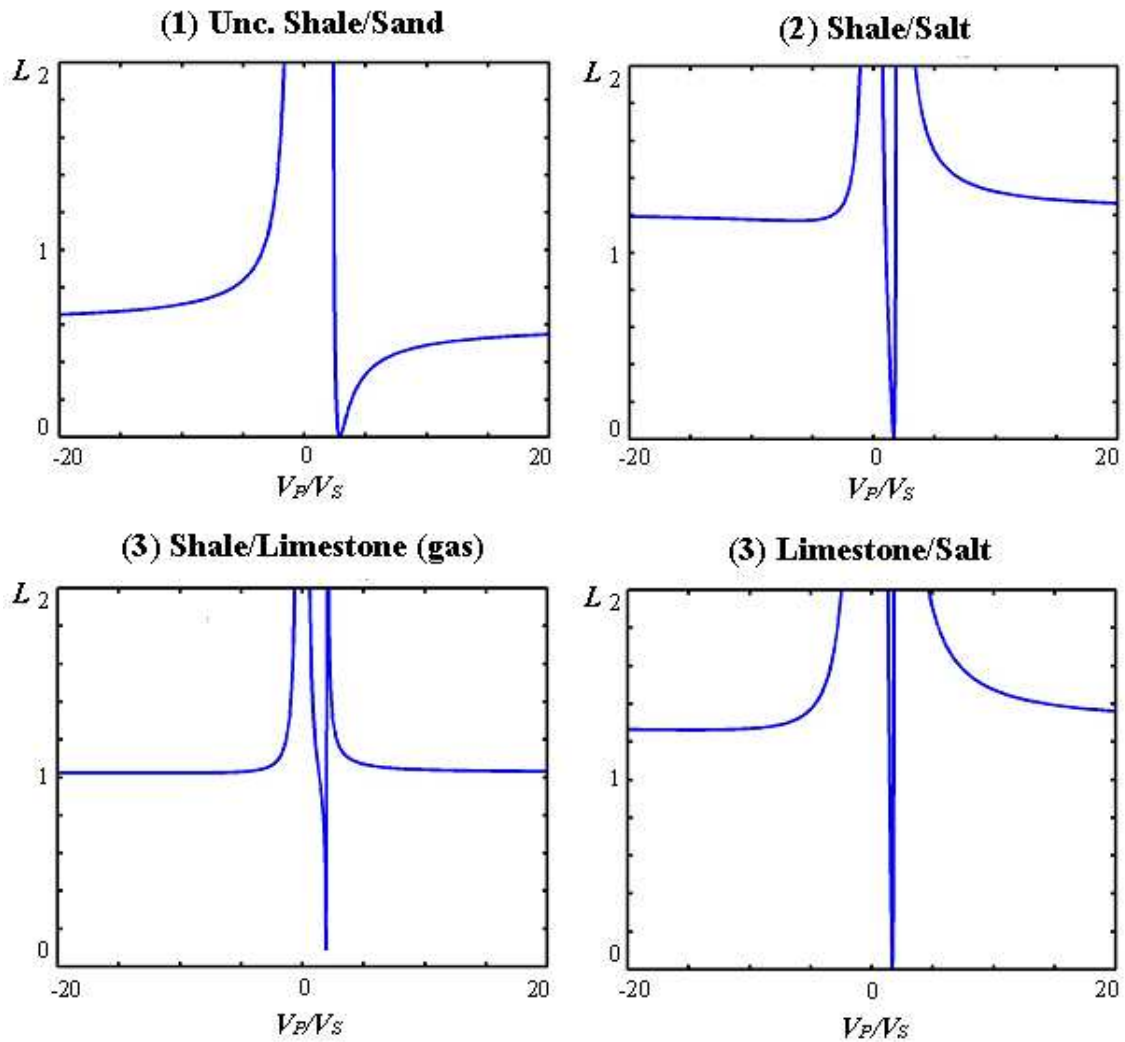


Fig. 2.5. Variation of the least-square cost function with values of the  $V_P/V_S$  ratio for the models described in Table 2.1. Each figure displays only one minimum value. Hence it shows that system of equations (2.8-2.11) has a unique solution.

## 2.4 Identification of Lithology

The estimated  $[V_P/V_S]_k$  ratio for each layer is given by

$$\left[\frac{V_P}{V_S}\right]_1 = \frac{V_P}{V_S} \left( \frac{2 - \frac{\Delta V_P}{V_P}}{2 - \frac{\Delta V_S}{V_S}} \right), \quad (2.17)$$

$$\left[\frac{V_P}{V_S}\right]_2 = \frac{V_P}{V_S} \left( \frac{2 + \frac{\Delta V_P}{V_P}}{2 + \frac{\Delta V_S}{V_S}} \right). \quad (2.18)$$

These equations were derived from the definitions of the relative elastic parameters and contrasts of the two layers, i.e.

$$\frac{\Delta V_P}{V_P} = 2 \frac{V_{P2} - V_{P1}}{V_{P2} + V_{P1}}, \quad (2.19)$$

$$\frac{\Delta V_S}{V_S} = 2 \frac{V_{S2} - V_{S1}}{V_{S2} + V_{S1}}, \quad (2.20)$$

$$\frac{V_P}{V_S} = \frac{V_{P1} + V_{P2}}{V_{S1} + V_{S2}}. \quad (2.21)$$

Poisson's ratio was given by

$$\sigma_k = \frac{\frac{1}{2} \left( \left[\frac{V_P}{V_S}\right]_k \right)^2 - 1}{\left( \left[\frac{V_P}{V_S}\right]_k \right)^2 - 1}. \quad (2.22)$$

Table 2.4 shows the estimated and actual values of the specific  $[V_P/V_S]_k$  ratio and Poisson's ratio for each layer in all models used in this chapter ( $k = 1$ , top layer; and  $k = 2$ , bottom layer). The estimated values of both  $[V_P/V_S]_k$  and Poisson's ratio appear to be good approximations of the actual values. Notice also in Table 2.4 that estimation of Poisson's ratio from the  $V_P/V_S$  slightly increases the probability of error due to its smallness and numerical operations. However, I here present

the tools to compute both of these values as Poisson's ratio is popularly used as a lithology discriminator and our estimations of this value are still accurate. An accurate estimation of the specific values of the  $V_P/V_S$  ratio and Poisson's Ratio for individual subsurface layers is important because it leads to the improvement of lithology identification in seismic exploration.

Table 2.4. Estimated and actual values for the specific  $(V_P/V_S)_k$  and Poisson's ratio for each layer in all models considered in this chapter. The estimated values approximate the actual ones with an error no greater than 1 percent.

Model	Layer	$V_P/V_S$		$\sigma$	
		Estimated	Actual	Estimated	Actual
1	Shale	4.2045	4.2022	0.4700	0.4710
	Sand	2.2033	2.2016	0.3703	0.3700
2	Shale	1.6528	1.6840	0.2113	0.2276
	Salt	1.6443	1.6757	0.2065	0.2234
3	Shale	1.6892	1.6840	0.2302	0.2276
	Limestone	1.7087	1.7054	0.2395	0.2380
4	Limestone	1.8281	1.8042	0.2865	0.2783
	Salt	1.7064	1.6757	0.2385	0.2234



## CHAPTER III

### AN APPLICATION TO FINITE-DIFFERENCE SIMULATIONS

#### 3.1 Introduction

To better simulate the performance of inversion algorithms, such as the one described in Chapter II, with real data it is necessary to develop synthetic models that represent the subsurface as genuinely as possible. Several approaches to numerically modeling the seismic response of the earth exist. They range from reflectivity methods (e.g., Frasier, 1970) to ray tracing methods (e.g., Chapman, 1971), to finite-difference techniques (e.g., Virieux, 1986; and Levander, 1988). Of all of these techniques of simulating elastic wave propagation through complex media, finite-difference modeling (FDM) is the most popular one as it can accurately predict travel times and amplitudes of primaries, multiples, converted waves, and diffractions.

The objective of this chapter is to validate the accuracy of the inversion scheme described in chapter II by using synthetic finite-difference-generated data. We will begin by reviewing the finite-difference techniques, and then we will apply them to our problem. Our review follows Appendix C of Ikelle and Amundsen (2003).

#### 3.2 Review of Finite-Difference Modeling

The propagation of seismic waves in the subsurface is mathematically represented by elastic wave equations. In petroleum exploration, seismic waves are normally

artificially generated in order to decipher subsurface lithologies, their structure, and their composition. By understanding the behavior of seismic waves, as described by the wave equation, exploration scientists are able to predict the results of a particular seismic experiment based on a preconceived model. In geophysical research, forward modeling refers to the generation of scaled models that represent reality given the characteristic parameters that represent such model. In Chapter I we introduced the idea that an isotropic elastic medium can be described by different parameters, such as its elastic moduli (Bulk and Shear modulus), or by their counterparts, seismic velocities and density. This idea is used by the wave equations to describe subsurface lithologies.

Finite-difference methods have a leading role in forward modeling in computational seismology because of their ability to accurately model wave propagation in laterally heterogeneous media. Unfortunately, explicit schemes are computationally expensive, requiring large amounts of computer memory to model exploration-scale problems. Currently only two-dimensional and small three-dimensional problems are feasible. By using higher order finite difference approximations of spatial and temporal derivatives, we can reduce computation time and memory requirements.

### 3.2.1 Elastic Wave Equations

The problem of simulating seismic surveys corresponds to the problem of solving the differential equations that control wave propagation in the earth under a set of initial, final, and boundary conditions. Extracted from (Levander, 1988), the differential equations to solve in 2-D media are the following:

$$\rho \frac{\partial v_x}{\partial t} = \frac{\partial \tau_{xx}}{\partial x} + \frac{\partial \tau_{xz}}{\partial z}, \quad (3.1)$$

$$\rho \frac{\partial v_z}{\partial t} = \frac{\partial \tau_{zx}}{\partial x} + \frac{\partial \tau_{zz}}{\partial z} , \quad (3.2)$$

$$\tau_{xx} = (\lambda + 2\mu) \frac{\partial u_x}{\partial x} + \lambda \frac{\partial u_z}{\partial z} , \quad (3.3)$$

$$\tau_{zx} = \mu \left( \frac{\partial u_x}{\partial z} + \frac{\partial u_z}{\partial x} \right) , \quad (3.4)$$

and

$$\tau_{zz} = (\lambda + 2\mu) \frac{\partial u_z}{\partial z} + \lambda \frac{\partial u_x}{\partial x} . \quad (3.5)$$

Equations (3.1-3.2) are the two-dimensional representation of the conservation of linear momentum equation, Newton's second law of motion. Equations (3.3-3.5) are a more specific representation of Hook's law for homogeneous isotropic 2-D media. In these equations,  $u_x$  and  $u_z$  are the horizontal and vertical displacement components, respectively;  $v_x$  and  $v_z$  are the horizontal and vertical particle velocity;  $\tau_{xx}$ ,  $\tau_{zx}$ , and  $\tau_{zz}$  are the different stresses;  $\rho$  is the mass density; and  $\lambda$  and  $\mu$  are the Lamé parameters. Together, equations (3.1-3.5) form a system of partial differential equations that describe wave propagation in the earth.

There does not exist an analytical solution to equations (3.1-3.5). Hence, numerical methods have been developed to account for this matter. Finite-difference computation has gained popularity as one of the most successful numerical techniques for solving these differential equations. It consists of numerical approximations of derivatives of differential wave equations.

### 3.2.2 Approximation

Finite-difference modeling operates by replacing the derivatives in an equation

with finite differences. Let us consider a function,  $f(x)$ . Its Taylor's theorem expansion about a point  $x$  can be written as

$$f(x+h) = f(x) + hf'(x) + \frac{h^2}{2}f''(x) + \frac{h^3}{6}f'''(x) + \dots \quad (3.6)$$

or, alternatively,

$$f(x-h) = f(x) - hf'(x) + \frac{h^2}{2}f''(x) - \frac{h^3}{6}f'''(x) + \dots \quad (3.7)$$

Here,  $h$  is the increment of  $x$ . If we truncate equations (3.6) and (3.7) after the second term, the first derivative of  $f(x)$  can be solved by the following approximations:

$$f'(x) \approx \frac{1}{h} [f(x+h) - f(x)], \quad (3.8)$$

and

$$f'(x) \approx \frac{1}{h} [f(x) - f(x-h)]. \quad (3.9)$$

The expressions contained in brackets on the right hand side of equations (3.8) and (3.9) are called finite differences. Alternatively, subtracting equation (3.9) from equation (3.8) leads to the second-order finite-difference approximation

$$f'(x) \approx \frac{1}{2h} [f(x+h) - f(x-h)]. \quad (3.10)$$

This approximation is more precise and favorable compared to the approximations in equations (3.8) and (3.9). By retaining terms in the Taylor expansion series, higher-order approximations are possible and precision increases. For instance, a fourth-order approximation, equation (3.11), can be accomplished by truncating equations (3.6) and (3.7); i.e.,

$$f'(x) \approx \frac{1}{2h} [f(x+h) - f(x-h)] - \frac{h^2}{6}f'''(x). \quad (3.11)$$

References to higher-order approximations can be found in Bayliss et al. (1986), Dablain (1986), and Levander (1988).

### 3.2.3 Implementation

The software used in this project requires finite-difference computations with respect to time and space. For the temporal derivatives, we use a second-order approximation given by

$$f'(t) \approx \frac{1}{2\Delta t} [f(t + \Delta t) - f(t - \Delta t)]. \quad (3.12)$$

For the spatial derivatives, we use a fourth-order approximation; i.e.,

$$f'(x) \approx \frac{1}{2\Delta x} [f(x + \Delta x) - f(x - \Delta x)] - \frac{\Delta x^2}{6} f'''(x), \quad (3.13)$$

where  $\Delta t$  is the temporal increment and  $\Delta x$  is the spatial increment.

In order to model seismic waves using finite-difference methods, there are some aspects we must consider, such as the grid and the boundary conditions. Let us look at these aspects in more detail.

#### 3.2.3.a The Grid

The finite difference software uses a staggered grid in both space and time (Virieux, 1986; and Levander, 1988), as seen in Figure 3.1, to update velocity and stress equations. The points at which the stresses are specified are halfway between the points at which the velocities are specified. So in one time step, both the velocity and the stress component are updated. The continuous velocity function is discretized into an average value for each square around a grid point.

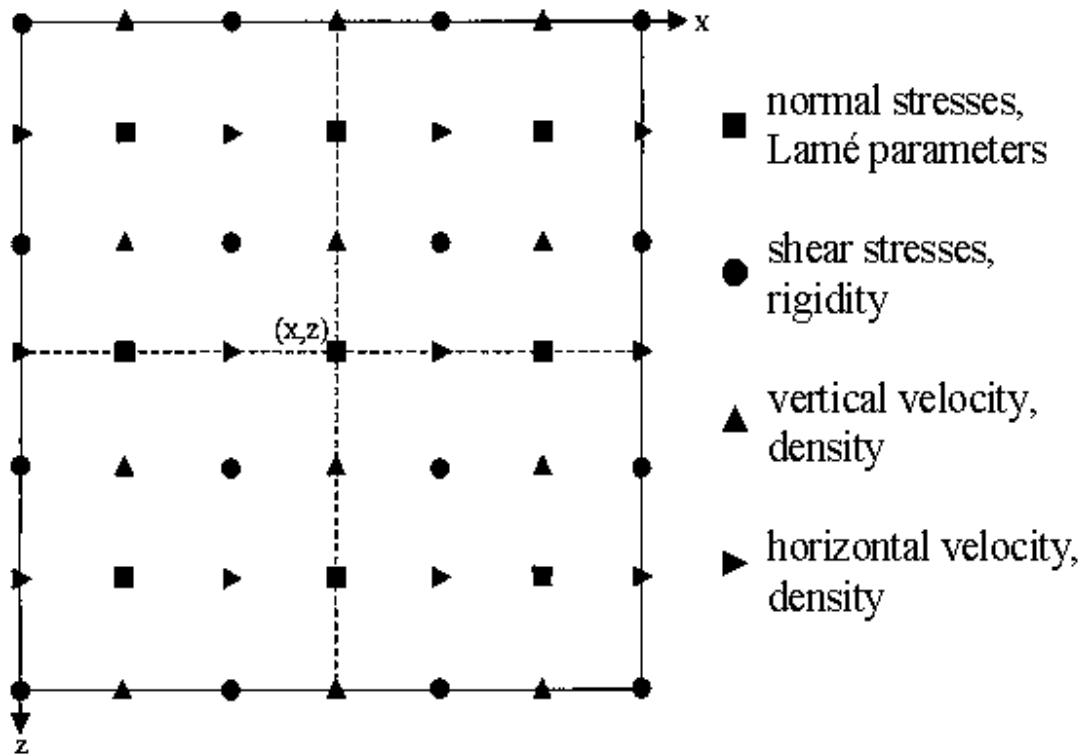


Fig. 3.1. Finite-difference staggered grid used to update the velocity and stress calculations (modified from Levander, 1988).

Understanding how the grid system works provides useful information for the creation of models. The size of the time step,  $\Delta t$ , is limited; information cannot be propagated across the grid faster than the grid velocity. The grid velocity is  $h/\Delta t$ , where  $h$  is the grid spacing. Hence the time step  $\Delta t$  must be bounded. The maximum time step, or stability condition, for two dimensions is given by

$$\Delta t \leq \frac{h}{v_{max}\sqrt{2}}, \quad (3.14)$$

where  $v_{max}$  is the maximum grid velocity.

One of the greatest benefits of using a staggered grid scheme is the stability for all values of Poisson's ratio. For our project, we need such stability for our algorithm

to work. Other benefits of a staggered grid, as discussed by Levander (1988), include the following:

- minimized grid dispersion and grid anisotropy,
- ability to simulate surface or buried sources.,
- ability to simulate free-surface boundary conditions.

This last item brings up the need for discussion of boundary conditions.

### 3.2.3.b Boundary Conditions

There are three different methods for boundary conditions: two are for non-reflecting conditions, and the other one is for reflecting conditions. Let us take a closer look at each one of these.

#### 1. Reflecting Boundaries:

Assume a flat surface and an incident wave which is propagated by the acoustic wave equation. The iterative finite-difference equation,  $\psi^{n+1}(z < 0) = \psi^n(z < 0) = 0$ , uses a grid which places a fictitious node or nodes outside the model. These nodes are initially zero and are kept at zero for all model times. All free-surface boundaries are reflecting.

#### 2. Non-Reflecting Boundaries:

There are two methods for non-reflecting boundaries. The first one is derived by factoring the one dimensional wave equation into two one-way wave equations. This factorization assumes that the primary wave direction is normal to the boundary. The difficulty of this method involves waves that arrive at

angles other than normal. The damping method, presented next, overcomes the angle dependent difficulty; it does not consider where the wave comes from. Furthermore, it is independent of the degree of approximation for the wave equation.

### 3. Damping Zone:

The alternative to boundary methods is a numerical damping zone, which reduces the wave strength over a grid region near the boundary. The idea is to slowly and smoothly apply a weight that will be effective in the aggregate. The smoothness is required for reducing the unwanted reflections within the damping zone. One method for implementation of the damping-zone boundary conditions is to store the weights in an array which matches the arrays used for the finite-difference scheme. In the interior of this array, the weights are set to unity. In this thesis, we use this method for non-reflecting boundaries.

#### 3.2.4 Discussion

After looking at what is necessary to know in order to apply a finite-difference algorithm, we should study the feasibility of finite-difference methods as it currently stands. Finite-difference methods have assumed a leading role in forward modeling in computational seismology because of their ability to accurately model wave propagation in laterally heterogeneous media. Unfortunately, explicit schemes are computationally expensive, requiring large amounts of computer memory to model exploration-scale problems.

Even though finite difference has proven to be promising in the field of forward subsurface modeling, it is still not flawless. Numerical dispersion prevents finite-difference methods from propagating waves over large distances. Also, interpretation



of numerical seismograms has shown to be a pitfall since its complexity increases as the complexity of the model increases. Something to note, though, is that nowadays analysis of numerical results is possible, but only because of powerful graphic tools which are used for data interpretation.

Finite-difference implementations of the wave equation are feasible and accurate as long as certain considerations are taken into account. First of all, high-order approximations tend to be more efficient than other schemes due to their speed and level of resolution (Virieux, 1986). As far as computational difficulties, taking advantage of no hardware-dependent optimization is of great aid (Villareal and Scales, 1997). In other words, considerable efficiency can be achieved by taking advantage of cache-oriented programming.

By keeping these considerations in mind when developing finite-difference models, we can assure a much more accurate and feasible scheme with exceptional results.

### 3.3 Inversion Algorithm

In chapter II, we developed the theoretical foundations for a quantitative inversion method of lithology identification that combines both  $P-P$  and  $P-S$  reflection data for isotropic media. This method aims to find the specific values of the Poisson's ratio of each rock formation in a half-space model for accurate discrimination. However, it is limited to nondipping reflectors in isotropic half-spaces.

Let us briefly remember how we derived this method. First of all, we looked at the linear behavior of both reflection coefficients,  $R_{PP}$  and  $R'_{PS}$ , for angles smaller than 35 degrees. We defined  $R'_{PS}$  as the normalized  $P-S$  reflection coefficient, given by equation (2.1). Several theoretical models were studied, graphing the reflection

coefficients for each model as a function of the squared sine of the incident angle. We also calculated a linear approximation for the small angles. Using this linear approximation (similar to that of Aki and Richards, 1980), we developed a nonlinear system of equations (equations 2.8-2.11), which allowed us to estimate the contrasts of  $P$ - and  $S$ -wave velocities, and of density, and the average  $V_P/V_S$  ratio. Separately, we derived the equations that describe the actual value of the  $V_P/V_S$  ratio for each lithology above and below the interface ( $[V_P/V_S]_k$ ) as a function of the seismic velocity contrasts and of the average  $V_P/V_S$  ratio. Consequently, we could estimate the specific Poisson's ratio of each of these formations, enabling their lithology identification.

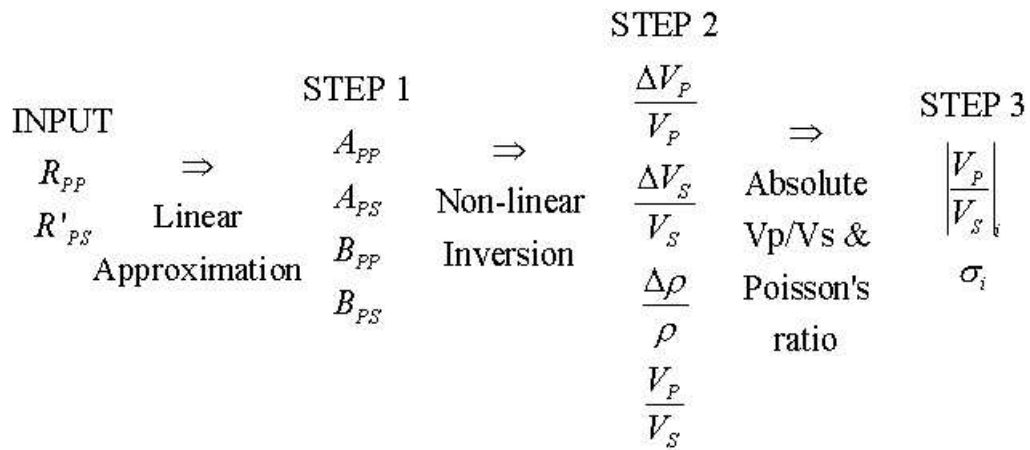


Fig. 3.2. Accurate and complete isotropic model that leads from a seismic data input (i.e.,  $R_{PP}$  and  $R'_{PS}$ ) to the specific values of Poisson's ratio ( $\sigma_i$ ) for each lithology forming an interface.

Figure 3.2 summarizes the steps of this algorithm. Let us see that it requires an input (i.e., the  $P - P$  and the normalized  $P - S$  reflection coefficients obtained from seismic data). After this input is processed, this algorithm returns an output (i.e., the specific values of Poisson's ratio for each rock formation). This process includes such steps as the linear approximation of the reflection coefficients, from which the

intercepts and gradients (i.e.,  $A_{PP}$ ,  $A_{PS}$ ,  $B_{PP}$ , and  $B_{PS}$ ) are estimated, followed by the nonlinear inversion of these parameters, which returns the elastic parameter contrasts  $\Delta V_P/V_P$ ,  $\Delta V_S/V_S$ , and  $\Delta\rho/\rho$  as well as the average  $V_P/V_S$  ratio.

For the rest of this chapter, we will follow the steps for the inversion algorithm, as described by Figure 3.2, applied to synthetic data. The first step will be to obtain the input to this process, namely the reflection coefficients. These coefficients will be extracted directly from the seismic data. Therefore, let us now generate synthetic seismic data using a finite-difference scheme.

### 3.4 Model Description

In order to generate finite-difference data, we first need to define the geological model to analyze. This description will include the geometry of the model as well as its elastic properties. We will also describe the acquisition geometry, as it is important for our scheme.

Table 3.1. Elastic parameters for an isotropic half-space similar to the shale/salt model from chapter II [ $V_P$  :  $P$ -wave velocity;  $V_S$  :  $S$ -wave velocity; and  $\rho$  : density].

Material	$V_P(Km/s)$	$V_S(Km/s)$	$\rho(g/cc)$
Shale	2.0834	1.2372	2.40
Salt	2.5000	1.4919	2.05

To focus our discussion, we will consider a simple isotropic half-space model similar to the shale/salt model (Model 2) used in Chapter II. Table 3.1 contains the elastic parameters of this rock formation. Although the specific elastic parameters of this model are not exactly the same as those of the shale/salt model from Chapter

II, Poisson's ratio has been kept the same. Therefore, our results should be similar to those of that model, helping us to analyze the accuracy of this inversion.

Figure 3.3 shows the geological model as well as the acquisition geometry used in this chapter. Let us recall that we are using an isotropic half-space model with shale overlying salt. The model also resembles an ocean bottom seismic (OBS) survey with receivers located near the sea floor (top of the shale). The source is seen as the incoming energy into the shale from a water explosion. It is located within the shale to avoid the effect of transmission of energy through the sea floor. This model uses absorbing boundary conditions on the sides, at the bottom, and at the top to eliminate multiples and maintain the focus of this work.

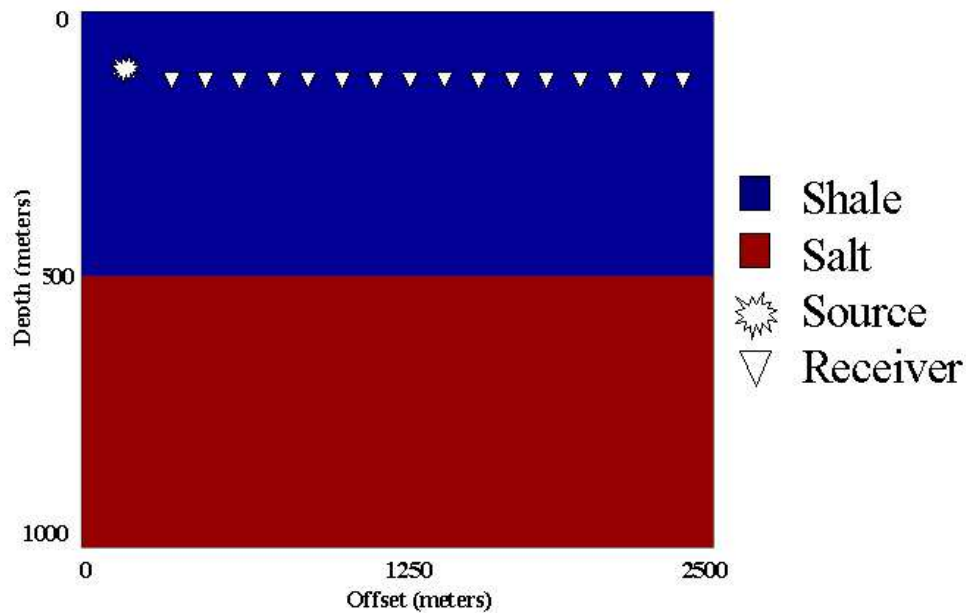


Fig. 3.3. Geological model and acquisition geometry to input in finite-difference code.

With this information, we can proceed to generate seismic data using our finite-difference code. Figure 3.4a shows the horizontal component of the normal stress ( $\tau_{xx}$ ). Here we can clearly appreciate two seismic events: a reflected  $P$ -wave ( $P-P$ )

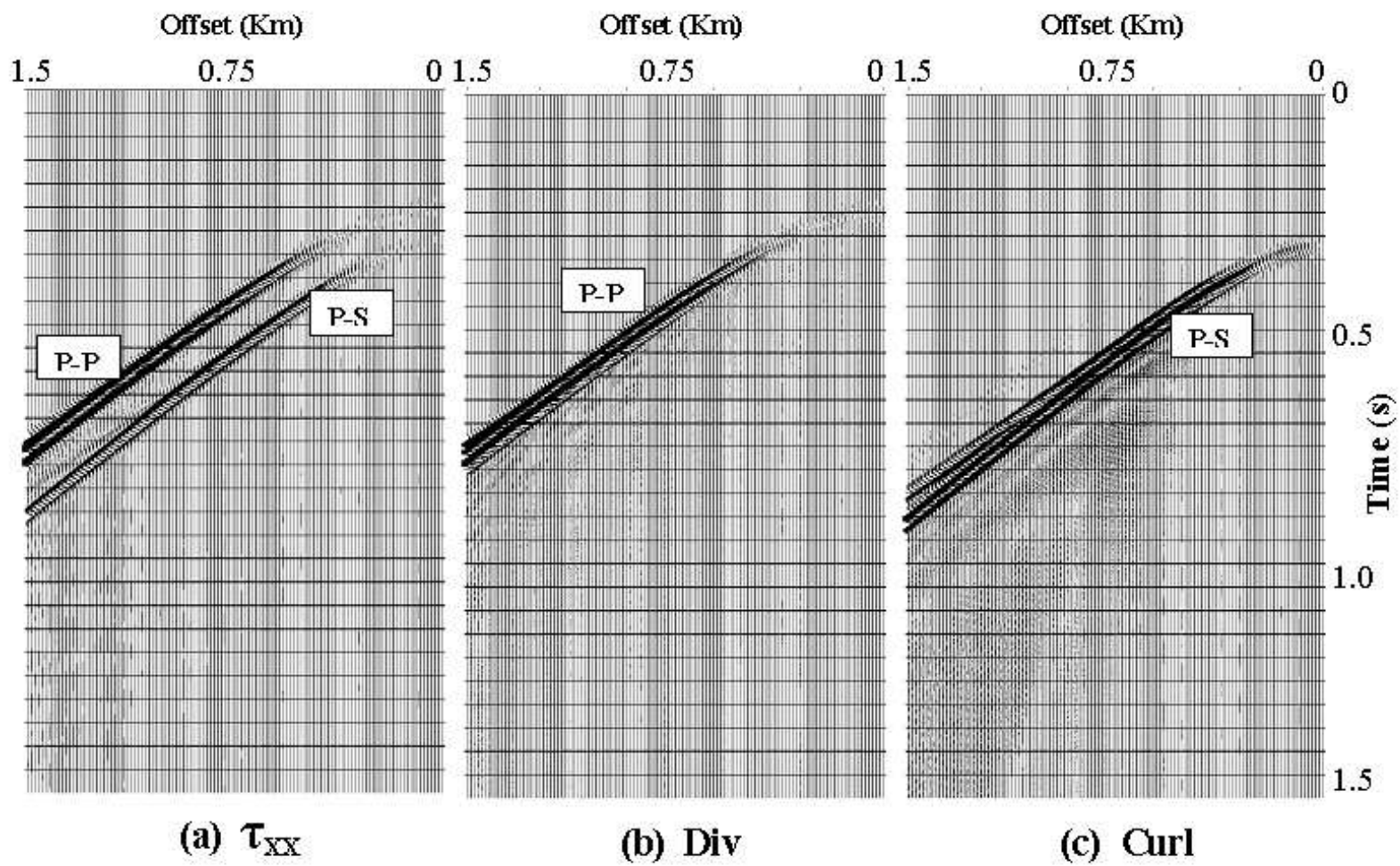


Fig. 3.4. Finite-difference generated seismic data showing: (a) Horizontal component of normal stress ( $\tau_{xx}$ ); (b) Divergence; and (c) Curl.

and a converted  $S$ -wave ( $P-S$ ). The  $P$ -wave arrives earlier than the  $S$ -wave, as it has a faster seismic velocity. The vertical component of the normal stress is not shown here since, given the nature of the source as well as the isotropic properties of the medium, it is equal to the horizontal component.

### 3.4.1 $P - P/P - S$ Separation

Although stress information clearly shows smooth, well-defined distinct seismic events (Figure 3.4a), it will be necessary to separate these two events into different shot gathers to facilitate picking the amplitudes for the reflection coefficients. The best way to do this separation is by calculating the divergence and the curl.

Before defining the divergence and the curl, we need to define the *del* operator ( $\nabla$ ).  $\nabla$  is defined in 3-D as a vector of spatial derivatives as follows:

$$\nabla = \begin{pmatrix} \frac{\partial}{\partial x} \\ \frac{\partial}{\partial y} \\ \frac{\partial}{\partial z} \end{pmatrix}. \quad (3.15)$$

The divergence is defined as the scalar product of the *del* operator ( $\nabla$ ) and the displacement vector field ( $\bar{u}$ ). In other words, it is the sum of the partial derivatives of each normal component of the displacement vector field with respect to the corresponding spatial coordinate. Equation 3.16 implements this definition in 3-D. Figure 3.4b shows the divergence of this data set. We can clearly see that now only one seismic event appears (i.e.,  $P - P$  reflection). Because of its definition (equation 3.16) that depends on normal stresses only, the divergence can be directly related to compressional information and thereby to the  $P - P$  reflection coefficient itself ( $R_{PP}$ ):

$$\text{div } \bar{\mathbf{u}} = \nabla \cdot \bar{\mathbf{u}} = \frac{\partial u_x}{\partial x} + \frac{\partial u_y}{\partial y} + \frac{\partial u_z}{\partial z}. \quad (3.16)$$

The curl is defined as the vector derivative of a vector field, such as displacement, and it is obtained by the cross product of the *del* operator and such vector field (equation 3.17). The curl of this data set is shown on Figure 3.4c. This figure shows only one seismic event (i.e.,  $P - S$  reflection). Unlike the divergence, according to equation (3.17) the curl is defined in terms of shear stresses only; therefore it can be associated with the  $P - S$  reflection coefficient ( $R_{PS}$ ).

$$\text{curl } \bar{\mathbf{u}} = \nabla \times \bar{\mathbf{u}} = \left( \frac{\partial u_z}{\partial y} - \frac{\partial u_y}{\partial z} \right) \mathbf{i} + \left( \frac{\partial u_x}{\partial z} - \frac{\partial u_z}{\partial x} \right) \mathbf{j} + \left( \frac{\partial u_y}{\partial x} - \frac{\partial u_x}{\partial y} \right) \mathbf{k}, \quad (3.17)$$

where  $\mathbf{i}$ ,  $\mathbf{j}$ , and  $\mathbf{k}$  are the unit vectors in the directions  $x$ ,  $y$ , and  $z$  of the orthonormal basis where the stress vector field is defined.

### 3.4.2 Extraction of Reflection Coefficients

Now that we have separated the wavefields, we can extract the  $P - P$  and the  $P - S$  reflection coefficients from the divergence and the curl, respectively, by picking the maximum amplitudes trace by trace. A reflection coefficient is actually defined as the amplitude of the corresponding seismic event. However, some calibration needs to be done. By the time a seismic wave reaches a geophone, a lot of energy has been lost due to a phenomenon referred to as geometrical spreading. The loss of energy due to geometrical spreading is proportional to the radius of the curvature of the propagating wavefront. In other words, as a consequence of the law of conservation, the energy density changes such that the surface integral of the considered wavefront is constant. In 2-D, as is this case, the amplitude is inversely proportional to the square root of the curvature of the propagating wavefront. Actually, because the radius of this curvature is directly related to the distance traveled, and therefore, to traveltime, the geometrical spreading factor can be defined in terms of traveltime. As

a result, we multiplied the reflection coefficients by the square root of the travelttime.

Once the reflection coefficients had been calibrated, we were able to compare them with the exact reflection coefficients as predicted by Zoeppritz' equations. Figure 3.5 and Figure 3.6 show the  $P - P$  and normalized  $P - S$  reflection coefficients, respectively. The exact reflection coefficients, as defined by Zoeppritz' solution, are shown in Figures 3.5a and 3.6a. Figures 3.5b and 3.6b show the estimated reflection coefficients as extracted from our seismic data. Let us recall that processing of the  $P - S$  reflection coefficient included one more step (i.e., normalization, as defined by equation 2.1). Figures 3.5d and 3.6d tell us that our estimation of the reflection coefficients returned accurate results, at least for small angles, which is what interests us at this point. Although our estimations do not behave smoothly, which we attribute to numerical dispersion of the finite-difference approximation, they maintain the linear trend that we look for at small angles of incidence. Therefore we consider these good results and are ready to input them into our inversion algorithm.

### 3.5 Inversion

As described earlier, by Figure 3.2, the inversion process developed in Chapter II requires the  $P - P$  and the normalized  $P - S$  reflection coefficients of a given geological interface as input. These reflection coefficients go through a series of steps, and in the end are expected to return the elastic parameters that describe the given model (i.e., Poisson's ratio of each lithology). In other words, we will use the concept of inverse modeling by using information from the finite-difference data (i.e., reflection coefficients) to identify the geological model that generated it. Let us begin by calculating the linear approximations for these reflection coefficients.



## P-P Reflection Coefficient

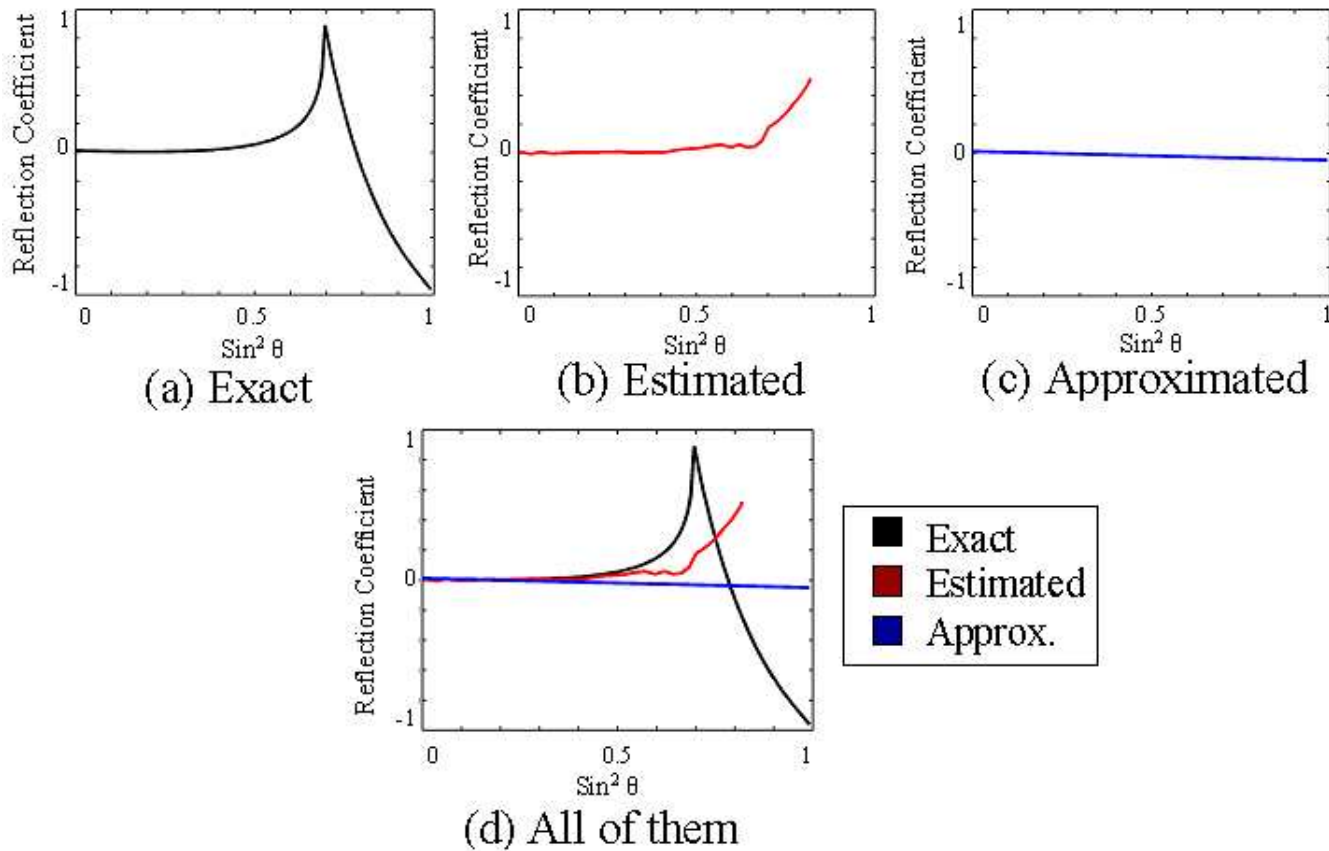


Fig. 3.5.  $P - P$  reflection coefficient of the shale/salt model [(a) exact from Zoeppritz' solution (black); (b) estimated from seismic data (red); (c) approximated by equations 2.2-2.7 (blue); (d) compilation of (a), (b), and (c)].

## Normalized P-S Reflection Coefficient

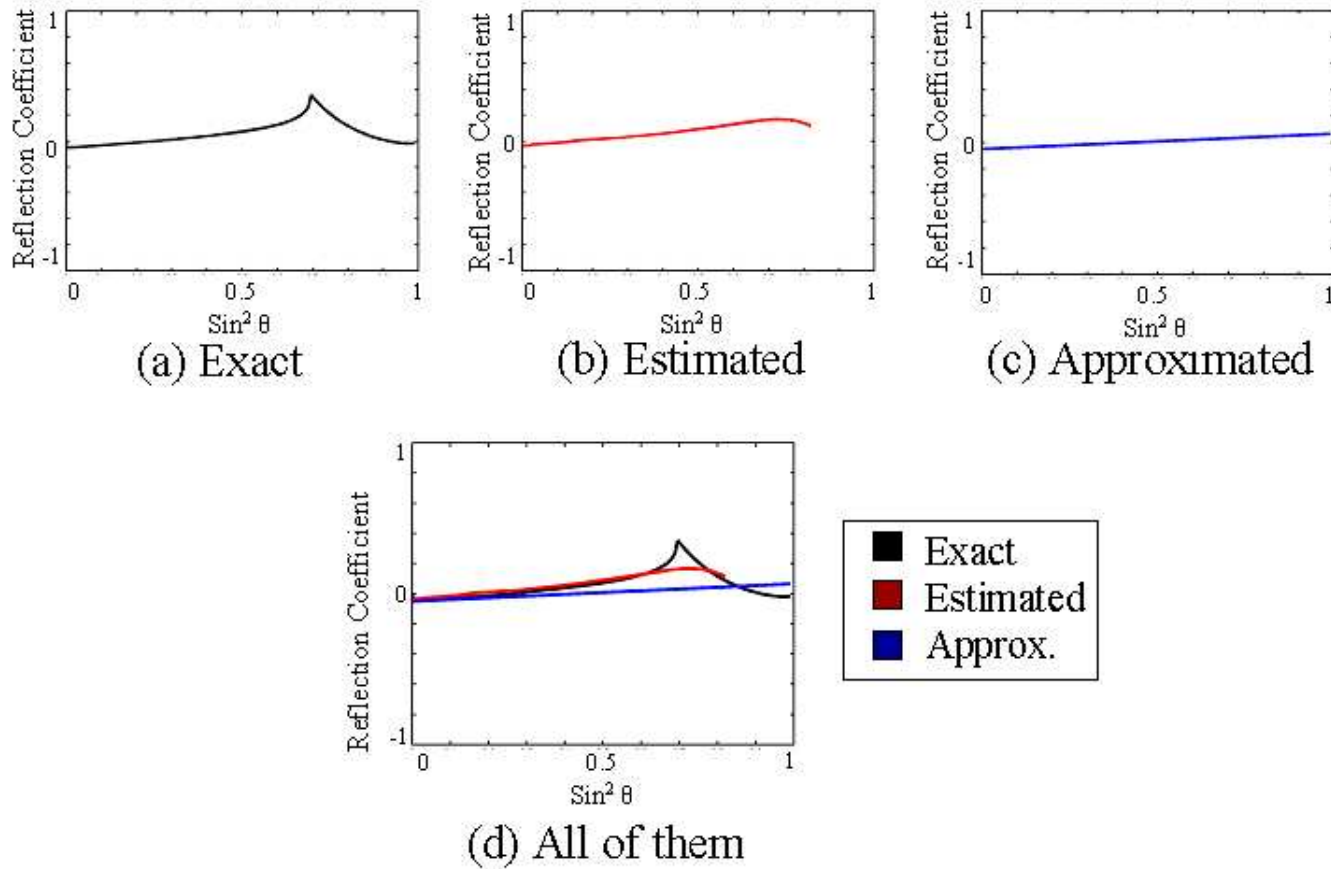


Fig. 3.6. Normalized  $P - S$  reflection coefficient of the shale/salt model [(a) exact from Zoeppritz' solution (black); (b) estimated from seismic data (red); (c) approximated by equations 2.2-2.7 (blue); (d) compilation of (a), (b), and (c)].

### 3.5.1 Step 1: Linear Approximation

Equations (2.2-2.7) provide a linear approximation for the  $P-P$  and normalized  $P-S$  reflection coefficients at small angles. We can apply these linear approximations to the reflection coefficients used in this chapter. Figures 3.5c and 3.6c show these linear approximations for both reflection coefficients. They are also validated in Figures 3.5d and 3.6d, as they appear to be good approximations of both the exact and the estimated reflection coefficients. The goal of this step is to estimate the intercepts and gradients (i.e.,  $A_{PP}$ ,  $A_{PS}$ ,  $B_{PP}$ , and  $B_{PS}$ ) of the reflection coefficients, which are shown in Table 3.2, as they will be the input for our next step.

Table 3.2. Intercepts and gradients [ $A_{PP}$ :  $R_{PP}$  intercept;  $B_{PP}$ :  $R_{PP}$  gradient;  $A_{PS}$ :  $R'_{PS}$  intercept; and  $B_{PS}$ :  $R'_{PS}$  gradient] for the shale/salt model described in Table 3.1.

Intercepts and Gradients	
$A_{PP}$	0.0123
$B_{PP}$	-0.0623
$A_{PS}$	-0.0500
$B_{PS}$	0.1166

### 3.5.2 Step 2: Nonlinear Inversion

Once the intercepts and gradients are obtained, we can proceed with the inversion. Equations (2.8-2.11) serve as a nonlinear system that will be solved iteratively as we did in Chapter II. The known values of this system are the intercepts and gradients stored in Table 3.2. We will use the same initial values used in Chapter II (i.e., 0.0001 for  $\Delta V_P/V_P$ ,  $\Delta V_S/V_S$ , and  $\Delta\rho/\rho$ , and 1.5 for the  $V_P/V_S$  ratio). Table 3.3 has the results of this inversion, and the actual values obtained directly from the elastic

parameters in Table 3.1. Again, we successfully obtained a unique solution with less than 1 percent error. The uniqueness of this solution is shown by the least-square cost function (Figure 3.7), which was calculated using equation 2.16.

Table 3.3. Estimated and actual values of  $\Delta V_P/V_P$ ,  $\Delta V_S/V_S$ ,  $\Delta\rho/\rho$ , and  $V_P/V_S$  for the shale/salt model used in this chapter. The less-than-1-percent error of approximation between estimated and actual values shows the accuracy of the inversion process.

Value	$\Delta V_P/V_P$	$\Delta V_S/V_S$	$\Delta\rho/\rho$	$V_P/V_S$
Estimated	0.1550	0.1601	-0.1304	1.6475
Actual	0.1818	0.1867	-0.1573	1.6795

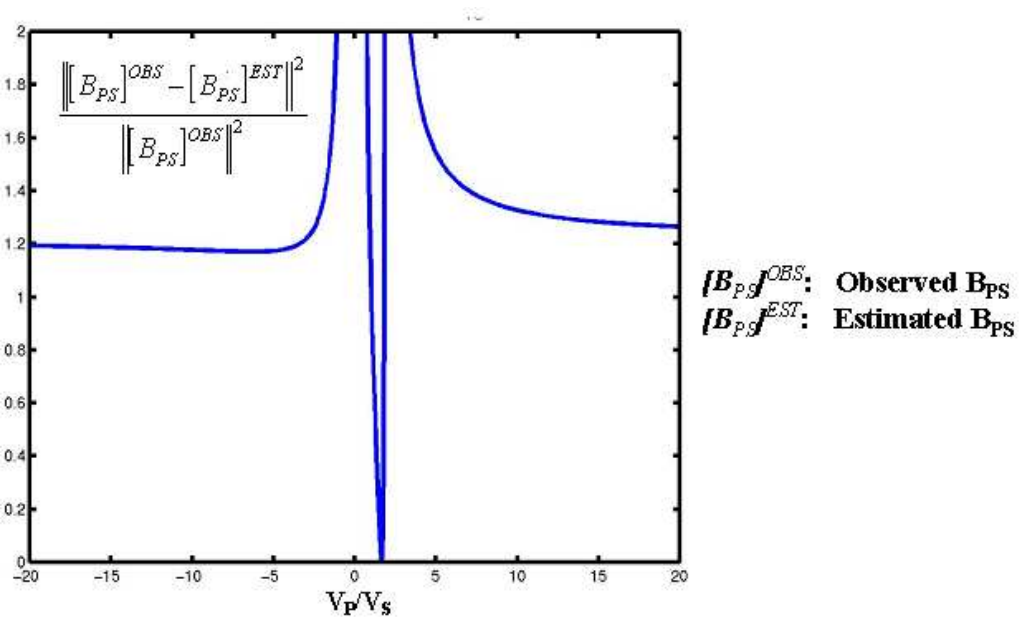


Fig. 3.7. Variation of the least-square cost function with values of the  $V_P/V_S$  ratio for the shale/salt model described in Table 3.1. This figure displays only one minimum value. Hence it shows that the problem has a unique solution.

### 3.5.3 Step 3: Specific Poisson's Ratio

Finally, we estimated the specific  $[V_P/V_S]_k$  ratio and Poisson's ratio for each layer in the shale/salt model used in this chapter ( $k = 1$ , shale; and  $k = 2$ , salt). Table 3.4 shows both the estimated and the actual values of these two parameters. The estimated values of both  $(V_P/V_S)_k$  and Poisson's ratio appear to be good approximations of the actual values, showing a successful and accurate estimation of the absolute Poisson's ratio for individual subsurface layers from finite-difference data, leading to the improvement of lithology identification in seismic exploration.

Table 3.4. Estimated and actual values for the specific  $(V_P/V_S)_k$  and Poisson's ratio for each layer in the shale/salt model considered in this chapter. The estimated values approximate the actual ones with an error no greater than 5 percent.

Layer	$V_P/V_S$		$\sigma$	
	Estimated	Actual	Estimated	Actual
1. Shale	1.6521	1.6840	0.2109	0.2276
2. Salt	1.6436	1.6757	0.2061	0.2235

## CHAPTER IV

### ANALYSIS AND GENERALIZATION FOR DIPPING INTERFACES

The ultimate goal of the method for lithology identification presented in this thesis is to be applied to real data to help increase the precision of hydrocarbon exploration. Most applications of AVO techniques target anomalies that have little or no dip, such as those caused by bright spots. However, seismic reflectors are seldom horizontally flat. Modern E&P explorations are conducted in very complex geological areas, which include severe dipping reflectors, such as salt flanks. Subsurface geologies normally possess structural complexities that are observed in the wide variety of shapes of the interfaces within them. They range from plain flat interfaces, to straight dipping reflectors, and even curved shapes such as anticlines and synclines. Because of the complexity that non-flat reflectors represent for AVO analyses, we will dedicate this chapter to study the effects and implications that dipping reflectors bring to our process.

In the previous chapters we have learned that AVO analysis can lead to estimating elastic parameters of subsurface materials. In fact, we developed an inversion algorithm that extracts such parameters, namely the actual value of Poisson's ratio. However, our study has assumed horizontally flat reflectors. AVO analyses need not to be restricted to such simple cases. The excuse behind this original assumption entails simplifying the problem to its very fundamental essence by eliminating unneeded complications, and thereby, maintaining the required focus. Yet, once the fundamentals of a problem have been treated, further research becomes a must. We have already

proven our inversion scheme to be valid for flat interfaces. Therefore, the following step of our research will be to generalize the governing equations for our inversion process to dipping reflectors.

In this chapter, we will show the derivations of such equations for dipping reflectors. We will also validate the equation for the most general case (i.e.,  $P - S$  reflection on dipping interfaces) by applying it to every other case considered in this chapter. And finally we will review the implications that a dipping reflector brings to our process and how to overcome such implications.

#### 4.1 Problems caused by dip

Let us begin by explaining why it is necessary to consider structural complexity in AVO analysis. J. P. Castagna in his 1993 AVO tutorial alluded to the unexploited tremendous potential of AVO analysis as a prospecting tool by attributing it partially to the wide variety of complications, problems, and pitfalls involved in isolating and interpreting offset-dependent reflectivity. He includes structural complexity of subsurface geologies as one of these complications. From the work by Resnick et al. (1987), Castagna lists a series of problems that the presence of dip can cause in AVO analysis. Some of these problems are:

1. errors in estimating parameters in AVO analysis that depend on reflection angle
2. mixing of information from different subsurface locations within a common mid-point gather
3. the dependence of normal-moveout corrections on reflector dip
4. interference of reflections by mispositioned events

If these problems are not taken care of, the dipping events can introduce flaws in AVO analysis that would lead to an erroneous interpretation.

Resnick et al. (1987) also points out why AVO analysis of dipping reflectors is more difficult. These reasons include:

1. reflection angle depends on reflector dip
2. the reflection point for a given event seen in a common midpoint (CMP) gather varies with source-to-receiver offset of  $x$ , moving updip with increasing offset
3. normal-moveout (NMO) corrections, which may be critical in AVO analysis, depend on reflector dip
4. mispositioned (i.e., unmigrated) seismic events interfere with one another

There exist remedies for all of these problems. The last three problems can be corrected with full prestack migration, therefore we will not treat them in depth. The first problem can be corrected by doing simple calculations that lead to interesting results. This is what we will focus on this chapter: the reflection angle, and thereby, the AVO response dependence on dip.

## 4.2 AVO Equations for Dipping Interfaces

Up to this point, our focus has been flat interfaces as illustrated in Figure 4.1a. In chapter II we used equations (2.2-2.3) to describe linear approximations to the reflection coefficients,  $R_{PP}$  and  $R'_{PS}$ , for small angles of incidence (i.e., less than 35 degrees). Let us now use the term AVO response,  $f_{AVO}$ , to refer to either one of these reflection coefficients. The incident angle is now represented by  $\theta_S$  and the reflection



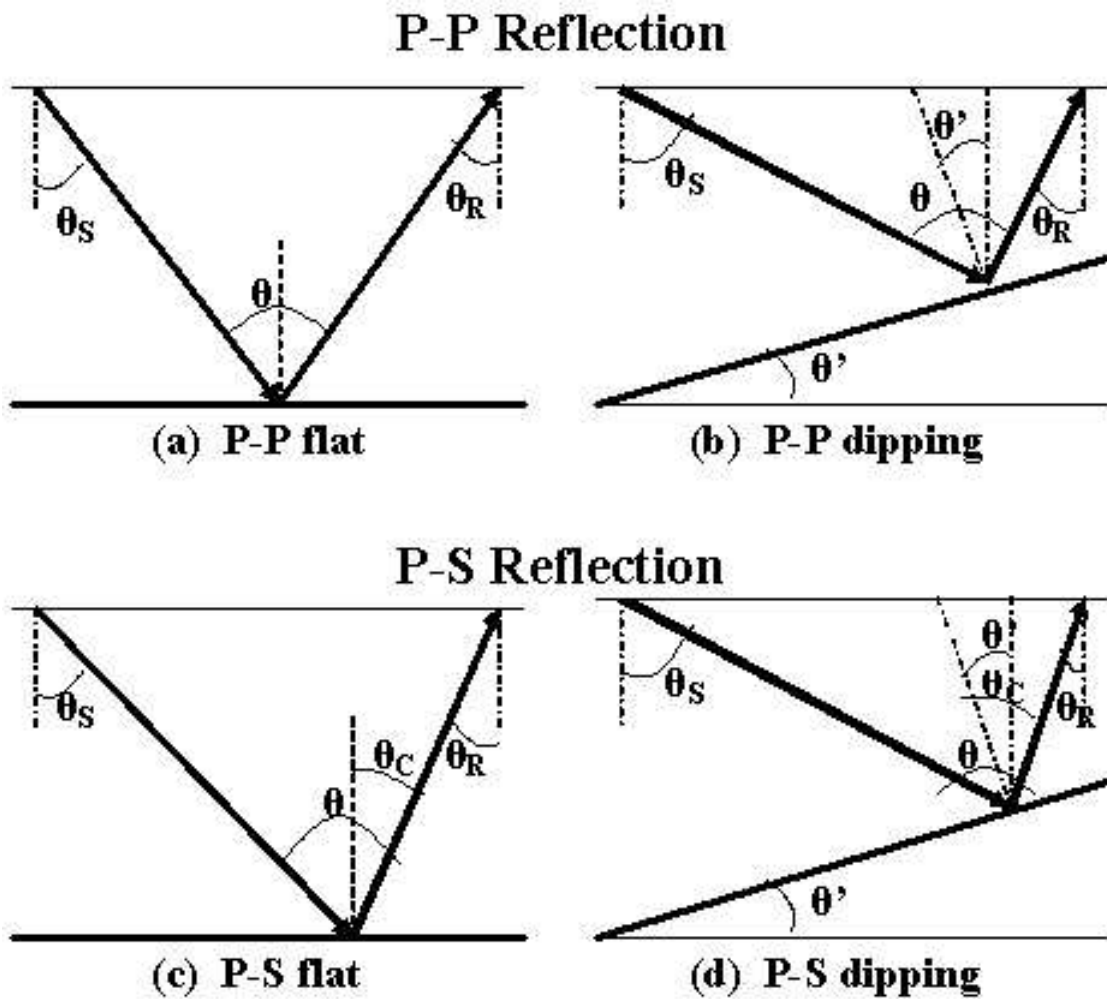


Fig. 4.1.  $P-P$  and  $P-S$  reflection at different interfaces. (a)  $P-P$  reflection on a flat interface, (b)  $P-P$  reflection on a dipping interface, (c)  $P-S$  reflection on a flat interface, and (d)  $P-S$  reflection on a dipping interface. [ $\theta_S$ : the incident angle,  $\theta_R$ : the reflection angle,  $\theta_C$ : the converted  $S$ -wave angle,  $\theta$ : the total reflection angle, and  $\theta'$ : the dipping angle.]

angle by  $\theta_R$ , as seen in Figure 4.1.  $\theta = \theta_S + \theta_R$  is the total reflection angle. Equation 4.1 rewrites equations (2.2-2.3) using this new terminology:

$$f_{AVO} = A + B \sin^2(\theta_S) . \quad (4.1)$$

#### 4.2.1 $P - P$ Reflection

We will first consider the problem of  $P - P$  reflection for dipping interfaces. Figure 4.1b shows such reflection. Here,  $\theta' = \theta_S - \theta_R$  is the angle of the dipping reflector. Notice that  $\theta'$  for a flat interface (Figure 4.1a) is zero. Furthermore, for  $P - P$  reflections on flat interfaces (Figure 4.1a),  $\theta_S$  and  $\theta_R$  are equal; whereas for dipping reflections (Figure 4.1b) they differ. We can observe that the difference between the incident angle and the reflection angle may imply consequences to our inversion scheme.

It can be shown that the  $P - P$  AVO response of a dipping interface is given by:

$$f_{AVO} = A + B \sin^2(\theta_S - \theta') , \quad (4.2)$$

where  $f_{AVO}$  returns  $R_{PP}$ ;  $A$  and  $B$  are the  $P - P$  intercept and gradient, respectively;  $\theta_S$  is the independent variable incident angle; and  $\theta'$  is the dipping angle. Notice that for  $\theta' = 0$ , equation 4.2 reduces to the original equation 4.1 for the reflection coefficients for a flat interface. Equation 4.2 can be written as a function of its independent variable,  $\theta_S$ , with coefficients in terms of the dipping angle  $\theta'$  in the following form:

$$f_{AVO} = A(\theta') + B(\theta') \sin^2 \theta_S + C(\theta') \sin 2\theta_S, \quad (4.3)$$

with

$$\begin{aligned} A(\theta') &= A + B \sin^2 \theta', \\ B(\theta') &= B \cos 2\theta', \\ C(\theta') &= -\frac{B}{2} \sin 2\theta'. \end{aligned}$$

Notice the presence of the new term  $C(\theta') \sin 2\theta$  in equation 4.3 as compared to equation 4.1. Because of the properties of the sine function and the relative small magnitude of  $C(\theta')$ , this term should not affect the linearity of  $f_{AVO}$  at small angles.

#### 4.2.2 Normalized $P - S$ Reflection

Let us now consider converted shear waves. According to Snell's Law, the angle of reflection of a converted  $S$ -wave is different than that of an incident  $P$ -wave (see Figure 4.1c). This phenomenon has effects on our analysis. Equation (4.1) for converted  $S$ -waves on a flat reflector can be written as follows:

$$f_{AVO} = A + B \sin^2 \left( \frac{\theta_S + \theta_C}{2} \right). \quad (4.4)$$

$\theta_C$ , the angle of the converted  $S$ -wave, which in this case is equal to  $\theta_R$ , is defined by Snell's Law as:

$$\theta_C = \sin^{-1} \left( \frac{V_2}{V_1} \sin \theta_S \right), \quad (4.5)$$

where  $V_1$  and  $V_2$  are the seismic velocities for incident ( $P$ -) and converted ( $S$ -) waves respectively.

In fact, we can even extend  $P - S$  reflection for a dipping interface at an angle

$\theta'$ , as we did for  $P - P$  reflection (Figure 4.1d). The resulting equation is:

$$f_{AVO} = A + B \sin^2 \left( \frac{\theta_S + \theta_C - \theta'}{2} \right). \quad (4.6)$$

$\theta_C$  is affected by  $\theta'$  as well:

$$\theta_C = \sin^{-1} \left( \frac{V_2}{V_1} \sin(\theta_S - \theta') \right). \quad (4.7)$$

### 4.3 Generalization of the AVO Equations

Equations (4.1), (4.2), (4.4), and (4.6) represent the AVO response for  $P - P$  reflection on a flat interface,  $P - P$  reflection on a dipping interface,  $P - S$  reflection on a flat interface, and  $P - S$  reflection on a dipping interface, respectively (recall Figure 4.1). In fact, equation (4.6) represents the most general case of AVO response as studied in this work. If the right assumptions are made, equation (4.6) can be reduced to equations (4.1), (4.2), and (4.4). For instance, if in (4.6) we make  $\theta' = 0$ , we obtain equation (4.4) ( $P - S$  reflection on a flat interface). Also, if we assume  $V_1 = V_2 = V_P$  in equation (4.7), equation (4.6) becomes equation (4.2) ( $P - P$  reflection on a dipping interface). Finally, if we combine this two assumptions, the resulting equation will be equation (4.1) ( $P - P$  reflection on a flat interface).

When looking at equation (4.6), we noticed that it obeys a more general statement. Let us remember the definitions for dipping angle and total reflection angle (see Figure 4.1). The angle of a dipping reflector is defined as  $\theta' = \theta_S - \theta_R$ , whereas the total reflection angle is  $\theta = \theta_S + \theta_R$ , which is the angle between the ray paths of the incident and reflected waves. From trigonometry, we can see that  $\theta_R = \theta_C - \theta'$ .

Based on these relations, we rewrite equation (4.6) as:

$$f_{AVO} = A + B \sin^2 \left( \frac{\theta}{2} \right). \quad (4.8)$$

This equation is a valid generalization for all of the different cases covered in this chapter as described by Figure 4.1. Equation (4.8) can be said to be the most general expression for the AVO response of a single interface (flat or dipping) to an incident P wave in a homogenous half space medium.

#### 4.4 Consequences of Dipping Reflectors

Our derivations have shown that the linear approximations for the  $P - P$  and  $P - S$  reflection coefficients shown in Chapter II for flat reflectors are still valid for dipping reflectors. We can still cast  $R_{PP}$  and  $R'_{PS}$  into intercepts and gradients, just like we did for nondipping reflectors. However, we observe that our intercepts and gradients (i.e.,  $A_{PP}$ ,  $A_{PS}$ ,  $B_{PP}$ , and  $B_{PS}$ ) are functions of the dipping angle. Therefore, the nonlinear system of four equations (2.4-2.7), which we used to solve for the contrasts of elastic parameters and for the  $V_P/V_S$  ratio, now has five unknowns. The fifth unknown is the angle of the dipping reflector,  $\theta'$ . In the next chapter, we will show that including a migration step into our process will allow us to find the fifth unknown.

## CHAPTER V

### AN INTEGRATED APPROACH TO MIGRATION AND AVO INVERSION

Previously, we have developed a nonlinear inversion algorithm that aims at estimating Poisson's ratio for each rock formation in a given geological model. Figure 3.2 summarizes the steps of this algorithm. Chapter III, in fact, gives a numerical application of this algorithm to synthetic seismic data following the steps in Figure 3.2. As explained in this figure, the input to the inversion algorithm is the reflection coefficients (i.e.,  $R_{PP}$  and  $R'_{PS}$ ), also known as AVO response ( $f_{AVO}$ , as learned in Chapter IV), extracted from seismic data. Chapter III, however, does not explain in much detail how these reflection coefficients are recovered from seismic data. Therefore, the objective of this chapter is to develop an algorithm that allows us to extract from seismic data the AVO response,  $R_{PP}$  and  $R'_{PS}$ , and to integrate this algorithm with the inversion algorithm developed in Chapter II for a complete estimation of Poisson's ratio directly from seismic data.

Our study will be founded on the work on linearized inversion by Ikelle et al. (1986 and 1988). Recovery of reflection coefficients from seismic data requires several considerations such as the effects of geometrical spreading, normal move-out, and  $P - S$  decomposition. Ikelle et al. (1986 and 1988) developed an algorithm that takes these considerations into account for reconstructing elastic parameters. We will make use of the basic concepts behind their inversion process and apply them to reconstruction of AVO response.

Chapters II and III of this thesis focus on simple idealizations of the earth, assuming isotropic homogenous one-dimensional half-spaces (i.e., horizontally flat interfaces between rock formations) for the models to be studied. The simplicity of a nondipping-reflector assumption ignores the structural complexity of realistic geological models observed in the diversity of shapes of interfaces within them. In chapter IV we learned that dipping reflectors introduce a new unknown to our system (i.e., the dipping angle). In this chapter we will apply the concepts developed in chapter IV for dipping reflectors. By standardizing the incident angle to the half-reflection angle,  $\theta/2$ , using the equations in chapter IV, we should be able to design a scheme that extracts the AVO response not only along a specific flat interface, but at any scattering point within the system in terms of its position, which complies for heterogeneity. This scheme will include a migration step, which will take care of the problem of estimating the dipping angle in order not to affect our inversion process for Poisson's ratio.

In this chapter we will describe the basic theory behind this algorithm, which follows that developed in Ikelle and Amundsen (2003). We generate more complicated synthetic seismic data and, lastly, we will explain how the algorithm can be applied to the seismic data for further research.

## 5.1 Linearized Inversion

One of the greatest challenges of seismic imaging has been to be able to reconstruct the model of the subsurface from data consisting essentially of primaries after it has been demultiplied and possibly deghosted. This reconstruction process constitutes an inverse problem, and it consists of discovering the physical parameters that most significantly contribute to the observed reflected field. To solve an inverse problem,

however, our first step is to select the physical laws that will allow us to predict seismic data for a given model of the subsurface. We refer to these physical laws as a forward modeling problem.

Here we will use a forward problem similar to that developed by Ikelle et al. (1986). Other models of the forward problem have been proposed. For instance, Cohen and Bleistein (1979) derived an algorithm for inversion of stacked data in the  $\omega - k$  domain. Clayton and Stolt (1981) gave a solution for unstacked data. However, we find Ikelle et al.'s solution to be the most cost-effective as it saves what could be perhaps large amounts of computing time by not requiring stacking of the data. This solution also has proven its efficiency and accuracy, as compared to that of Clayton and Stolt's, which considers the predicted scattered wave field,  $\delta P$ , as original data, leaving room open for numerical artifacts.

In chapter II, we describe a way of reconstructing elastic parameters from AVO response. This AVO response was described by the linearized form of the reflection coefficients,  $R_{PP}$  and  $R'_{PS}$ , under the assumption that the reflecting interface was horizontally flat. In chapter IV we extended this theory to the cases in which the reflecting interface is no longer horizontally flat. Unfortunately, seismic acquisition does not record directly the AVO response. So we first need to recover the AVO responses from the data before we reconstruct elastic parameters. Therefore the first goal in this section will be to derive a way of reconstructing AVO response from seismic data.

### 5.1.1 Forward Problem

Let us begin by setting a forward model similar to that used by Ikelle et al. (1986). Their formulation is actually based on that by Tarantola (1984); though they



differ in that the inverse iterative solution of Tarantola is explicit in the  $\omega - k$  domain. We will, instead, use a more simplified and more general form for the equation of the forward problem than that derived by Ikelle et al. (1986):

$$\delta P(k_x, k_y, k_h, \omega) = \frac{1}{Q(k_x, k_y, k_h, \omega)} \int_{-\infty}^{\infty} dk_z \delta(k_z - q) f_{AVO}(\theta, k_x, k_y, k_z) . \quad (5.1)$$

Equation (5.1) is a generalization of the linearized forward problem for acoustic scattering restricted to the case in which the 3-D acquisition geometry consists of a series of 2-D multioffset profiles whose source and receivers are located at the same depth, as is our case. Later we will extend this formula to the problem of interest of this thesis:  $P - P$  and  $P - S$  scattering in elastic media. Equation (5.1) solves for a pressure wavefield,  $\delta P$  in terms of position and the source frequency,  $\omega$ . Notice that, because this solution has been derived in  $\omega - k$  domain, positions are given in terms of wavenumbers ( $k_x, k_y, k_z$ , and  $k_h$ ).  $k_x, k_y$ , and  $k_z$  are the corresponding Fourier transform of the orthonormal coordinates ( $x, y$ , and  $z$ );  $k_h$  is the Fourier transform of the half-offset defined as,

$$h = \frac{x_r - x_s}{2} , \quad (5.2)$$

where  $x_r$  and  $x_s$  are the horizontal receiver and source positions respectively. If a solution in time and space is required, it will be necessary to take the inverse Fourier transform for a proper solution.

The forward problem of acoustic scattering (equation 5.1) essentially contains three terms: the geometrical spreading term represented by  $1/Q$ , the phase term represented by  $q$ , and the amplitude-variations-with-offset term, or AVO response, represented by  $f_{AVO}$ . Let us take a closer look at each of these terms.

### 5.1.1.a Geometrical Spreading

The term  $1/Q$  describes the amplitude attenuation of waves propagating through a background medium. It only depends on the velocity of the background medium. It is defined as,

$$Q = Q(k_x, k_y, k_h, \omega) = \frac{V_P^2}{\sigma_0 \omega^2} q_r q_s \sqrt{q_0} , \quad (5.3)$$

where  $V_P$  is the acoustic velocity of the background medium;  $\sigma_0$  is the specific volume of the background medium;  $\omega$  is the source frequency;  $q_s$  and  $q_r$  are the wavenumber travel times between source point and scattered point and between receiver point and scattered point, respectively; and  $q_0$  is defined in terms of  $q_s$  and  $q_r$  as follows:

$$q_0 = \frac{q_{sx}^2}{q_s^3} + \frac{q_{rx}^2}{q_r^3} , \quad (5.4)$$

$$q_{sx} = \frac{\omega}{V_P} \sqrt{1 - \frac{V_P^2 (k_x - k_h)^2}{4\omega^2}} , \quad (5.5)$$

$$q_{rx} = \frac{\omega}{V_P} \sqrt{1 - \frac{V_P^2 (k_x + k_h)^2}{4\omega^2}} . \quad (5.6)$$

The main objective of the geometrical spreading term is to remove the so-called evanescent waves. We also need to overcome the numerical artifacts that arise near the boundary between nonevanescant energy and evanescent energy. To do so we will introduce a new parameter,  $\epsilon$ , slightly smaller than one, in the computation of  $Q$  as follows:

$$Q = Q(k_x, k_y, k_h, \omega) = \frac{V_P^2}{\sigma_0 \omega^2} q_{r\epsilon} q_{s\epsilon} \sqrt{q_0} , \quad (5.7)$$

where

$$q_{s\epsilon} = \frac{\omega}{V_P} \sqrt{1 - \epsilon \frac{V_P^2 [(k_x - k_h)^2 + (k_y - k_h^0)^2]}{4\omega^2}}, \quad (5.8)$$

$$q_{r\epsilon} = \frac{\omega}{V_P} \sqrt{1 - \epsilon \frac{V_P^2 [(k_x + k_h)^2 + (k_y + k_h^0)^2]}{4\omega^2}}, \quad (5.9)$$

and

$$k_h^0 = k_y \frac{q_{rx} - q_{sx}}{q_{rx} + q_{sx}}. \quad (5.10)$$

The optimum value of  $\epsilon$  can be chosen by trial and error. Let us recall that the geometrical spreading term only depends on the velocity of the background medium, which can be estimated using the obvious conditions for equations (5.8-5.9) to remain real:

$$\frac{\omega^2}{V_P^2} > \frac{(k_x - k_h)^2 + (k_y - k_h^0)^2}{4}, \quad (5.11)$$

$$\frac{\omega^2}{V_P^2} > \frac{(k_x + k_h)^2 + (k_y + k_h^0)^2}{4}. \quad (5.12)$$

### 5.1.1.b Phase or Traveltimes

Phase  $q = q_s + q_r$  describes the travel times between the source point and the scattered point and between the receiver point and the scattered point. This term represents the migration step in the forward problem described by equation (5.1). Migration is highly dependent on the geometry of a geological model. Therefore, if structural complexities such as dipping reflectors are present, migration will take care of the problem. Because dipping angles are solved for during this step, they no longer appears as an independent variable in the wave field equation (5.1). With the geo-

metrical spreading factor, phase governs the wave propagation through a background medium. Notice that  $q$  depends only on the velocity of the background medium, as does the geometrical spreading. Therefore, for linearized forward and inverse problems of acoustic scattering we only need to know the velocity of the background medium,  $V_P$ , to solve these two problems.

### 5.1.1.c AVO Response

The function  $f_{AVO}$  is the amplitude radiation pattern. It describes how amplitudes of seismic data vary with offset. We can define the acoustic AVO response as:

$$f_{AVO} = f_{AVO}(\theta, k_x, k_y, k_z) = \Delta I(k_x, k_y, k_z) \cos^2 \frac{\theta}{2} + \Delta V(k_x, k_y, k_z) \sin^2 \frac{\theta}{2}. \quad (5.13)$$

Notice that  $f_{AVO}$  is the only term of the scattering field that depends on the reflection angle,  $\theta$ . It does not depend on the dipping angle, as this problem is taken care of by the migration step.  $\Delta I$  and  $\Delta V$  are the acoustic impedance contrast and velocity contrast at the scattering point  $(x, y, z)$ . Equation (5.13) shows a relative independence between these two parameters, which is important in setting up an inverse problem because we want to describe the earth by using parameters that are as independent as possible.

### 5.1.2 Forward Problem in Elastic Media

Let us consider  $v_l(x_r, y_r, t; x_s, y_s)$ , which denotes the  $l$ -component of the particle velocity at the receiver  $(x_r, y_r, z_r = 0)$  and at time  $t$  for a source  $(x_s, y_s, z_s = 0)$ . Let us also keep focus on the case in which 3-D multioffset data consist of a series of

parallel 2–D profiles. If the medium is elastic, it can be shown that the scattered field of  $v_l$ ,  $\delta v_l$ , due to a point force in the  $k$ –direction can be decomposed into four fields as follows:

$$\begin{aligned} \delta v_l(k_x, k_y, k_h, \omega) &= U_{kl}^{(PP)}(k_x, k_y, k_h, \omega) + U_{kl}^{(PS)}(k_x, k_y, k_h, \omega) \\ &+ U_{kl}^{(SP)}(k_x, k_y, k_h, \omega) + U_{kl}^{(SS)}(k_x, k_y, k_h, \omega) . \end{aligned} \quad (5.14)$$

Because we are assuming OBS data, which due to the nature of its source does not generate incident  $S$ –waves, we will concentrate only on the  $U_{kl}^{(PP)}$  and  $U_{kl}^{(PS)}$  scatter fields.

Also in solid media, in which we consider  $P - P$  and  $P - S$  scattering, sources as well as receivers can be oriented along a particular direction. Therefore, in addition to characterizing the seismic response by traveltime, geometric spreading, and AVO, we need to add a fourth component, which describes source and receiver polarizations.

### 5.1.2.a For $P - P$ Scattering

Let us rewrite equation (5.1) for the  $P - P$  scattering case in elastic media:

$$U_{kl}^{(PP)}(k_x, k_y, k_h, \omega) = \frac{M_{kl}(k_x, k_y, k_h, \omega)}{Q(k_x, k_y, k_h, \omega)} \int_{-\infty}^{\infty} dk_z \delta(k_z - q) f_{AVO}^{(PP)}(\theta, k_x, k_y, k_z) . \quad (5.15)$$

The main difference between  $P - P$  scattering and acoustic scattering lies on the addition of a polarization matrix,  $M_{kl}$  that describes source and receiver polarizations, as a fourth component of seismic response. If we normalize the  $P - P$  scattering field by the element  $M_{kl}$  of the polarization matrix; i.e., replace  $U_{kl}^{(PP)}$  by  $U^{(PP)}$ , which is defined as,

$$U^{(PP)} = \frac{U_{kl}^{(PP)}}{M_{kl}} , \quad (5.16)$$

then the  $P - P$  scattering becomes equivalent to acoustic scattering; the same linearized inversion algorithms can be used for both the acoustic scattered field and the  $P - P$  scattered field.

Another difference is that isotropic solids, case that we consider here, are characterized by three parameters (e.g., density and the two Lamé parameters), whereas the acoustic media can be characterized by two parameters only. However, this difference does not affect our processing.

As far as the AVO response itself for  $P - P$  scattering, it is equivalent to that of acoustic scattering. After eliminating the very large offsets (i.e., higher powers of sin function), whose effect does not interest us in this study, we can rewrite the amplitude variation with offset for  $P - P$  scattering as:

$$f_{AVO}^{(PP)} = A_{PP}(k_x, k_y, k_z) + B_{PP}(k_x, k_y, k_z) \sin^2 \frac{\theta}{2} . \quad (5.17)$$

### 5.1.2.b For $P - S$ Scattering

The general form of  $P - S$  scattering is not much different from  $P - P$  scattering. We can write the forward problem of  $P - S$  scattering as

$$U_{kl}^{(PS)}(k_x, k_y, k_h, \omega) = \frac{M'_{kl}(k_x, k_y, k_h, \omega)}{Q(k_x, k_y, k_h, \omega)} \int_{-\infty}^{\infty} dk_z \delta(k_z - q') f_{AVO}^{(PS)}(\theta', k_x, k_y, k_z) . \quad (5.18)$$

Notice that similarly to  $P - P$  scattering (equation 5.15),  $P - S$  scattering also includes a polarization matrix,  $M'_{kl}$ . In addition, the  $P - S$  AVO response also differs from that of the acoustic case as follows:

$$f_{AVO}^{(PS)} = \sin \theta' \left[ A_{PS}(k_x, k_y, k_z) + B_{PS}(k_x, k_y, k_z) \sin^2 \frac{\theta'}{2} \right] . \quad (5.19)$$

Observe the weighing factor,  $\sin \theta'$ , in equation (5.19). Because of these two

differences, a normalization for the  $P - S$  scattering is required; though, it will be different than the  $P - P$  normalization. Let us normalize the  $P - S$  scattering field by  $\sin \theta'$  and by the element  $M'_{kl}$  of the polarization matrix; i.e., replace  $U_{kl}^{(PS)}$  by  $U^{(PS)}$ , which is defined as follows:

$$U^{(PS)} = \frac{U_{kl}^{(PS)}}{M'_{kl} \sin \theta'}, \text{ for } \theta' > 0. \quad (5.20)$$

With the new amplitude radiation pattern,

$$\bar{f}_{AVO}^{(PS)} = A_{PS}(k_x, k_y, k_z) + B_{PS}(k_x, k_y, k_z) \sin^2 \frac{\theta'}{2}, \quad (5.21)$$

the  $P - S$  scattering becomes equivalent to acoustic scattering. Therefore, the same linearized inversion algorithms can be used for the  $P - P$  and  $P - S$  scattered fields, keeping in mind that the interpretation of the parameters will be different, according to the definitions of  $P - P$  and  $P - S$  intercepts and gradients (equations 2.4-2.7).

### 5.1.3 Inversion for $f_{AVO}$

In the previous section we developed the forward problem for  $P - P$  and  $P - S$  scattering. We concluded that both scattering modes have equivalent forms and therefore we could use the same inversion algorithm for the two of them. Let us now use  $U$  to refer to either  $U^{(PP)}$  or  $U^{(PS)}$ .

The problem of reconstructing AVO response from seismic data can be derived in the same way that Ikelle et al., 1986, did for reconstructing elastic parameters. Unlike their system, ours deals with a single parameter inversion (i.e.,  $f_{AVO}$ ). Fortunately, this difference does not fundamentally modify the algebra of our solution; it actually simplifies it.

Since both, the geometrical spreading factor as well as the phase factor, depend

only on the background velocity, they both can be predicted as long as an appropriate background velocity model is chosen. Therefore, let us define  $\bar{U}$  as the scattered field corrected for geometrical spreading:

$$\bar{U}(k_x, k_y, k_h, \omega) = Q(k_x, k_y, k_h, \omega)U(k_x, k_y, k_h, \omega) . \quad (5.22)$$

Now, after having taken the proper considerations, we can develop a least-squares solutions for reconstructing AVO response, similar to that used by Ikelle et al., 1986 for reconstructing elastic parameters. We will define the best AVO response,  $f_{AVO}$ , of a scattered field,  $\bar{U}_{pred}$ , which minimizes the misfit between  $\bar{U}_{pred}$ , the predicted scattered field from  $f_{AVO}$ , and the observed scattered field,  $\bar{U}_{obs}$ . In other words, the best reconstructed AVO response in a least-squares sense is defined as the model  $f_{AVO}$ , which minimizes the quadratic functional

$$F(f_{AVO}) = \|\bar{U}_{obs} - \bar{U}_{pred}\|^2 + \|f_{AVO}\|^2 . \quad (5.23)$$

## 5.2 Implementation

In Chapter III, we generated synthetic seismic data to prove the validity of the nonlinear inversion scheme for elastic parameters developed in Chapter II. The model used was, however, simple. But it respected the assumptions set in Chapter II. In Chapters IV and V, not only have we generalized the scheme to more structurally complex models, taking into account dip of subsurface reflectors, but we have developed the theory for an algorithm for recovering the reflection coefficients, or AVO response, from seismic data as required by the inversion for elastic parameters (refer to Figure 3.2).

For the rest of this chapter, we will explain how to implement this new algorithm



to synthetic models of the earth. Therefore, we will begin by using finite-difference modeling to generate seismic data. Our initial procedure will be similar to that followed in Chapter III.

### 5.2.1 Model Description

The first step to generate finite-difference data is to define the geological model to analyze. We will generate data for a four-layered model with an embedded elliptical salt body (Figure 5.1). The different layers possess complexities such as straight dip, light thickness, sharp diffractors, and curved surfaces such as that of the salt.

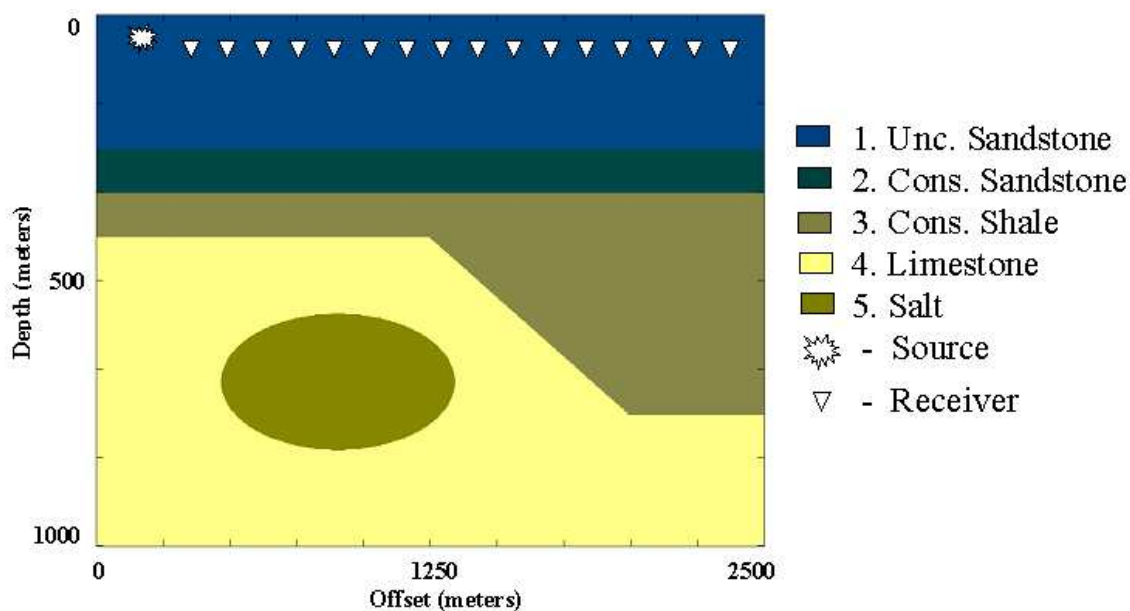


Fig. 5.1. Complex geological model and acquisition geometry to generate finite-difference data.

Table 5.1 contains the elastic parameters of each of the five rock formations included in this model, as well as their specific Poisson's ratio. We have made sure that the stratigraphic distribution of these five lithologies conforms to possible real

geological settings in oceanic crust. Their values of Poisson's ratio also comply with those given in Table 1.1. Complexities in the physical properties of this model also exist (i.e., negative acoustic and elastic impedance contrast, as well as negative density contrasts).

Table 5.1. Elastic Parameters for a heterogeneous complex geological model [ $V_P$  :  $P$ -wave velocity;  $V_S$  :  $S$ -wave velocity;  $\rho$  : density; and  $\sigma_k$  : Poisson's ratio].

$k$	Lithology	$V_P(Km/s)$	$V_S(Km/s)$	$\rho(g/cc)$	$\sigma_k$
1	Unc. Sandstone	2.00	1.00	1.50	0.33
2	Cons. Sandstone	2.50	1.50	1.70	0.22
3	Cons. Shale	2.25	1.10	2.10	0.34
4	Limestone	2.65	1.30	2.40	0.34
5	Salt	3.00	1.60	0.95	0.30

Figure 5.1 also shows the acquisition geometry used in this chapter. The model also resembles a 2-D OBS survey with receivers located near the sea floor (top of the unconsolidated sandstone). The source is seen as the incoming energy into the shale from a water explosion. We have used 121 receivers with a spacing of 12.50m between them, covering a total offset of 1500m. We shot as many times as the number of receivers we have from each receiver position. This model uses absorbing boundary conditions on the sides, at the bottom, and at the top to eliminate free-surface multiples and ghost and maintain the focus of this work.

### 5.2.2 Preliminary Results

Once the geological model and acquisition geometry have been defined and gathered, we proceed to generate seismic data using our finite-difference code. We have

set the receivers to collect stress information ( $\tau$ ). We have generated 121 shots, one from each receiver position. Figure 5.3 shows the horizontal component of the normal stress ( $\tau_{xx}$ ) for five distinctive shots. We have chosen to show these gathers because each one possesses unique characteristics. The two end shots (i.e., 0m and 1500m) as well as the mid-offset shot (i.e., 750m) are classical examples of shot gathers, from which it is convenient to extract information. The other two (i.e., 400m and 1100m) uniquely show the effects of the salt body and of the dipping reflector as both of these are hit at normal incidence. Figure 5.2 shows the different seismic events recorded. Although arrival times can be used in Figure 5.3 for identification of seismic events, we would rather wait to separate the  $P-P$  and  $P-S$  data for a more clear perspective of the scattering events.

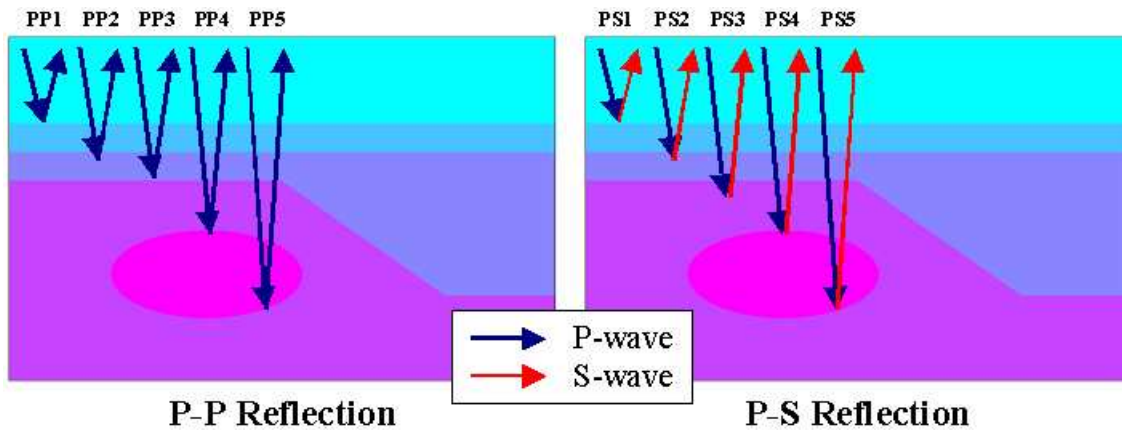


Fig. 5.2.  $P-P$  and  $P-S$  reflections recorded in the seismic data.

With stress information only, it is difficult to tell apart the different seismic events taking place. Therefore, it is necessary to separate the main two scattering modes,  $P-P$  and  $P-S$ , to facilitate extraction the AVO response. The best way to do this separation is by calculating the divergence and the curl defined by equations (3.16) and (3.17), respectively. Figure 5.4 shows this separation of data

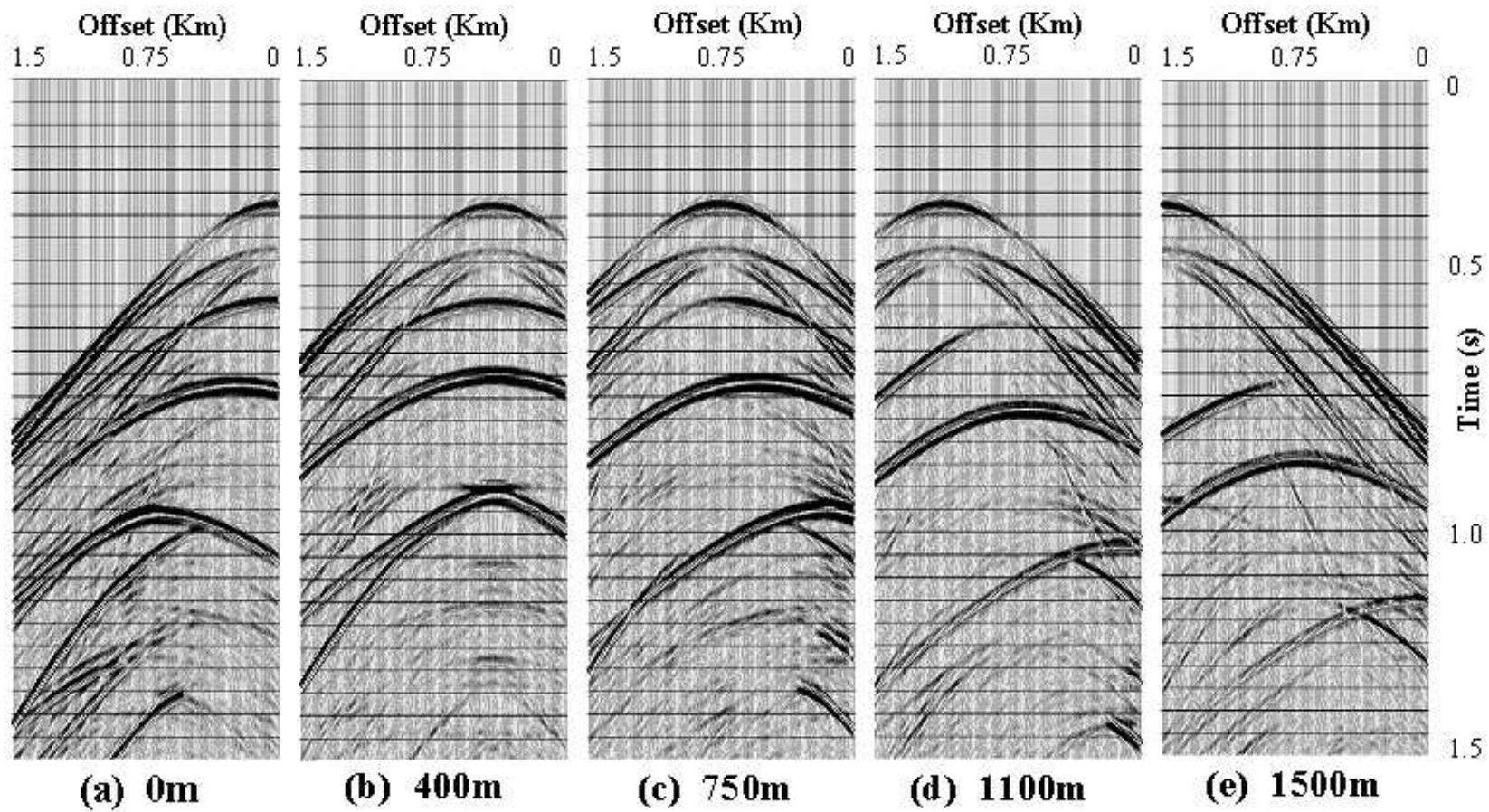


Fig. 5.3. Finite-difference generated seismic data showing the horizontal component of normal stress ( $\tau_{xx}$ ) for the model shown in Figure 5.1 at different source locations: (a) 0m; (b) 400m; (c) 750m; (d) 1100m; and (e) 1500m.

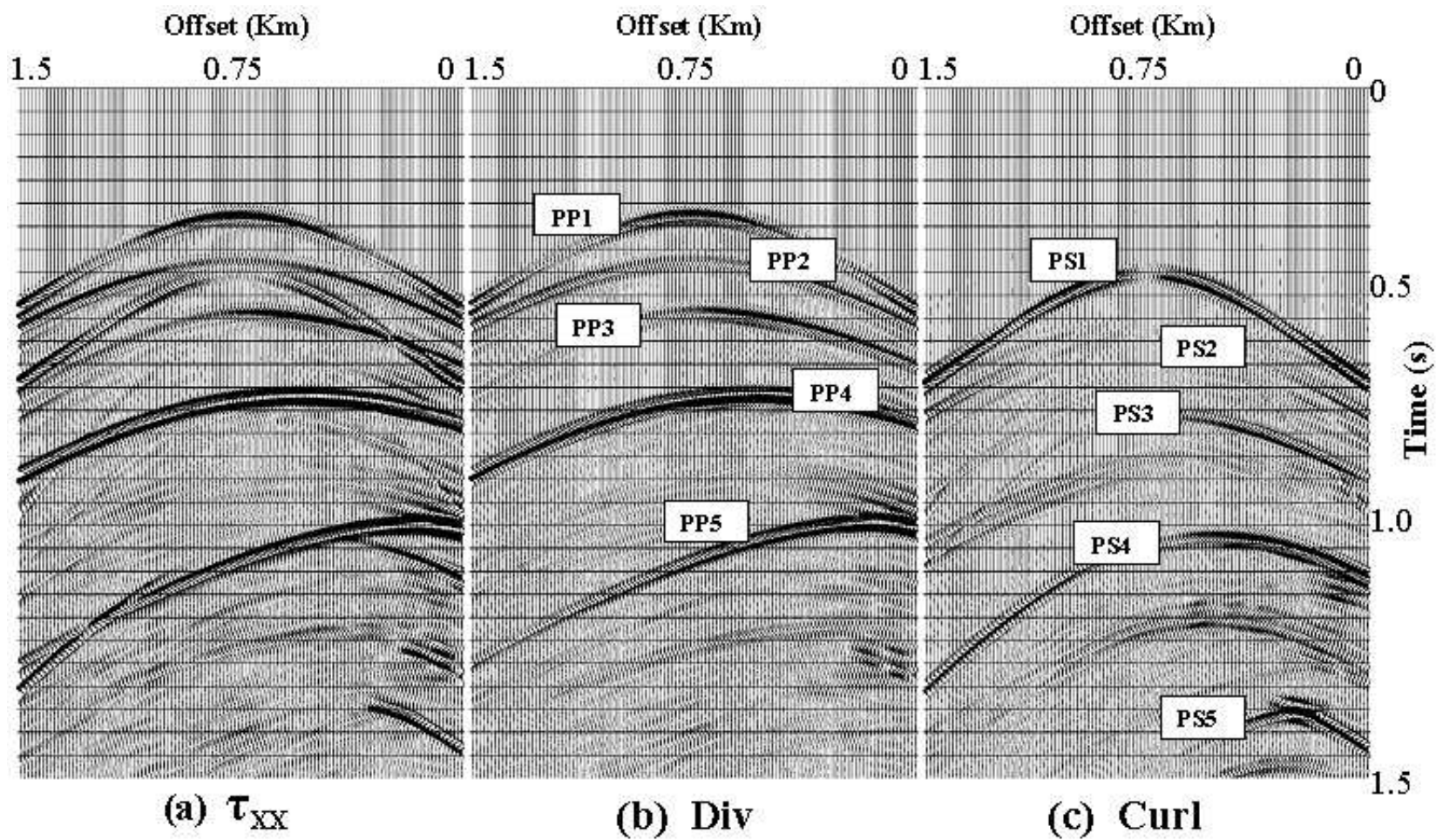


Fig. 5.4.  $P - P$  and  $P - S$  separation with source location at 0m, showing: (a) Horizontal component of normal stress ( $\tau_{xx}$ ); (b) Divergence ( $P - P$ ); and (c) Curl ( $P - S$ ).

for the half-offset shot gather (i.e., 750m). Notice that using the divergence and the curl (Figure 5.4b and 5.4c) it is now easier to identify the different seismic events described by Figure 5.2. By splitting  $P - S$  from  $P - P$  events, we can now appreciate a clearer distinction between them.

### 5.3 Recommendations for Processing and Inversion of Data

Up to this point, we have developed the theory behind an inversion algorithm that recovers the AVO response of seismic data. We have also generated such data in order to test our algorithm. The next step is to process the data before it is ready to apply the AVO extraction algorithm.

We recommend to follow the steps for seismic data processing followed by Ikelle et al. (1986, 1988) and summarized by Figure 5.5. First of all, we need to group all of the data into common-depth-point (CDP) gathers. Also, it will be necessary to correct for normal move-out (NMO). Once this processing is done, some pretreatment of the data might be necessary before applying the linearized inversion. In particular, an  $f - k$  filter may be applied to suppress noise caused by numerical dispersion of the finite-difference modeling code. In addition, a classical deconvolution may be performed to keep the source function relatively uniform in space and close to a spike.

In order to be ready to apply the linearized inversion, one has to choose a background model. Commonly, this model may be chosen to be constant throughout the system. However, this might bring artifacts to our results. Ikelle et al., 1988, suggest that a velocity model that varies with depth may be more realistic and appropriate. In their work, Ikelle et al. found that the accuracy of the linearized inversion algorithm greatly depends on the keenness to choose a background model. Once this model has been chosen, the least-squares scheme described by equation (5.23) can be

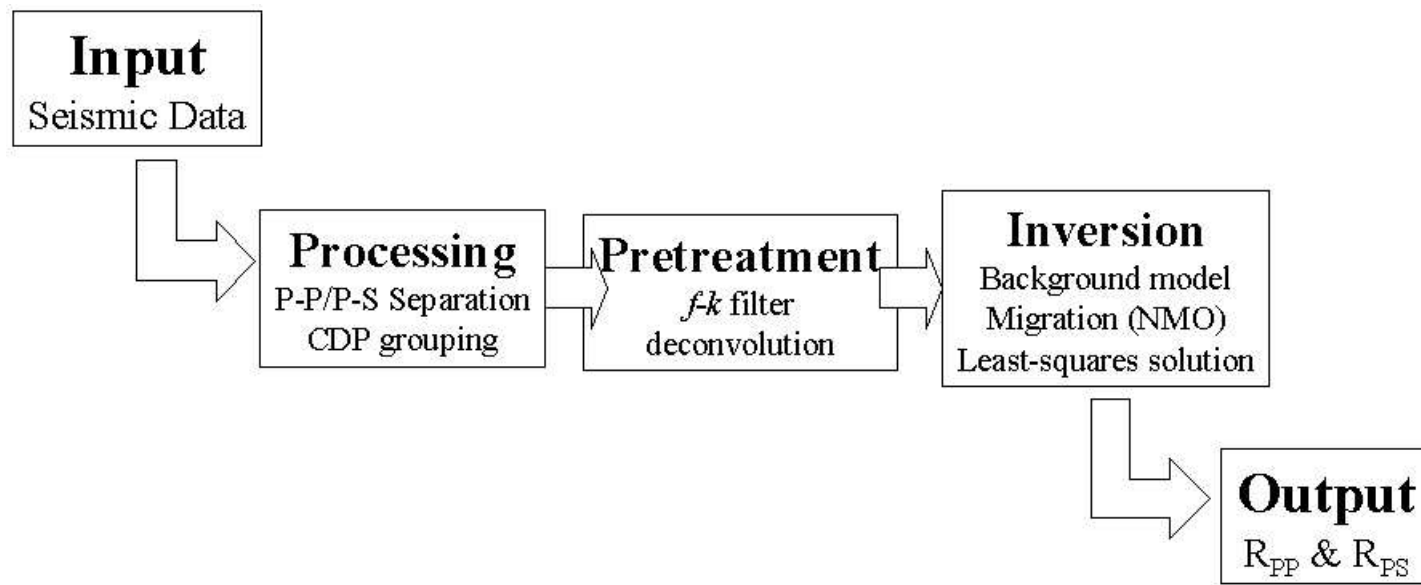


Fig. 5.5. Inversion scheme that uses migration to calculate the reflection coefficients,  $R_{PP}$  and  $R_{PS}$  directly from seismic data.

carried out. This step will require previous correction for geometrical spreading as well as migration. When performing migration, the angle of dipping reflectors will be found, and the nonlinear inversion from Chapter II will have only four unknowns again. The most optimum values of  $f_{AVO}$  should be the ones that will be used in our nonlinear inversion for elastic parameters. From this point on the procedure will be similar to that followed in Chapter III.

Let us observe that the recovered AVO response will be in the form of a function of the reflection angle,  $\theta$ , for a given scattering location within the geological model. This observation is very important because now we will be able to solve for Poisson's ratio at any location in the subsurface, considering the heterogeneous nature of real geological formations.

With this final step we would be proving our nonlinear inversion algorithm for elastic parameters (Chapter II), as well as our linearized inversion for (Chapter V), to be a thorough and accurate process that leads from rough seismic data to the identification of subsurface lithologies based on the identification of Poisson's ratio and of the AVO response of each rock formation and every interface within them.



## CHAPTER VI

### CONCLUSIONS

We have proposed a new AVO analysis, which simultaneously uses  $P - P$  and  $P - S$  reflection data. Furthermore, this AVO analysis allows us to estimate directly the actual value of Poisson's ratio instead of its contrast within an interval, as most previous methods of classical AVO. We have proven that this method is accurate and consistent when applied to isotropic half-space models. These are the key steps of our method

1. *Normalization:* The first step is the normalization of the  $P - S$  reflection coefficient, which consists of the division of  $R_{PS}$  by  $\sin\theta$ , where  $\theta$  is the incident angle. This normalization is, of course, valid for angles greater than zero. By normalizing  $R_{PS}$ , we avoid dealing with the absence of converted  $S$ -waves near normal incidence and enhance the linear behavior of  $R'_{PS}$ , similar to that of  $R_{PP}$ .
2. *Linear Approximation:* The linear properties of the reflection coefficients at small angles allow us to cast  $R_{PP}$  and  $R'_{PS}$  into intercepts and gradients. Using these intercepts and gradients, it is feasible to set up a system of equations with four unknowns.
3. *Nonlinear Inversion:* We have been able to use a nonlinear iterative scheme, which helps us estimate uniquely from the intercepts and gradients of  $P - P$  and  $P - S$  data, the elastic parameters  $\Delta V_P/V_P$ ,  $\Delta V_S/V_S$ ,  $\Delta\rho/\rho$ , and specially the  $V_P/V_S$  ratio.

Finding the  $V_P/V_S$  ratio provided the missing link to estimating the actual value of Poisson's ratio of each rock formation in a half-space model based on the reflection coefficients  $R_{PP}$  and  $R'_{PS}$ .

Secondly, we have theoretically shown the existence and validity of an inversion system that finds these reflection coefficients, also referred to as AVO response ( $f_{AVO}$ ), directly from the seismic data. This inversion exploits the theory of the linearized forward problem for the description of scattered seismic energy in the earth. Here, we also consider the effects of structural complexities, namely dipping reflectors. However, by introducing a migration step, we solve for the problem of dipping interfaces. Furthermore, the recovered AVO response will be in the form of a function of the reflection angle,  $\theta$ , for a given scattering location within the geological model. This observation tells us that we can solve for Poisson's ratio at any location in the subsurface, therefore, complying with the heterogeneous nature of real geological formations.

Therefore, by combining these two schemes, we have developed a complete system that leads to estimation of Poisson's ratio at any position in the earth directly from seismic data alone.

## REFERENCES

- Aki, K. I., and Richards, P. G., 1980, Quantitative seismology - Theory and methods, Volume I: W. H. Freeman and Company.
- Bayliss, A., Jordan, R. E., LeMesurier, B. J., and Turkel, E., 1986, A fourth-order accurate finite-difference scheme for the computation of elastic waves: Bulletin of the Seismological Society of America, **76**, 1115–1132.
- Bortfeld, R., 1961, Approximation to the reflection and transmission coefficients of plane longitudinal and transverse waves: Geophys. Prosp., **9**, 485–502.
- Carcuz, J., 2001, A combined AVO analysis of P-P and P-S reflection data: 71<sup>st</sup> Ann. Internat. Mtg., Soc. Explor. Geophys., Expanded Abstracts, 323-325.
- Castagna, J. P., 1993, AVO analysis - Tutorial and review, *in* Castagna, J. P., and Backus, M. M., Eds., Offset-dependent reflectivity - Theory and practice of AVO analysis: Society of Exploration Geophysicists, Investigations in Geophysics Series, 8, 3–36.
- Chapman, C. H., 1971, On the computation of seismic ray travel times and amplitudes: Bulletin of the Seismological Society of America, **61**, 1267–1274.
- Clayton, R. W., and Stolt, R. H., 1981, A Born-WKBJ inversion method for acoustic reflection data: Geophysics, **46**, 1559–1567.
- Cohen, J. K., and Bleistein, N., 1979, Velocity inversion procedure for acoustic waves: Geophysics, **44**, 1077–1087.
- Dablain, F. A., 1986, The application of higher-order differencing to the scalar wave equation: Geophysics, **51**, 54–66.

- Engelmark, F., 2000, Using converted shear waves to image reservoirs with low-impedance contrast: *The Leading Edge*, **19**, 600–603.
- Ensley, R. A., 1984, Comparison of P- and S-wave seismic data: A new method for detecting gas reservoirs: *Geophysics*, **49**, 1420–1431.
- Fatti, J. L., Smith, G. C., Vail, P. J., Strauss, P. J., and Levitt, P. R., 1994, Detection of gas in sandstone reservoirs using AVO analysis: A 3-D seismic case history using the geostack technique: *Geophysics*, **59**, 1362–1376.
- Frasier, C. W., 1970, Discrete time solution of plane P-SV waves in a plane layered medium: *Geophysics*, **35**, 197–218.
- Garotta, R., Granger, P., and Darius, H., 2002, Combined interpretation of PP and PS data provides direct access to elastic rock properties: *The Leading Edge*, **21**, 532–535.
- Ikelle, L. T., and Amundsen, L., 2003, *An introduction to petroleum seismology*: Society of Exploration Geophysicists.
- Ikelle, L. T., Diet, J. P., and Tarantola, A., 1986, Linearized inversion of multioffset seismic reflection data in the  $\omega - k$  domain: *Geophysics*, **51**, 1266–1276.
- 1988, Linearized inversion of multioffset seismic reflection data in the  $\omega - k$  domain: Depth-dependent reference medium: *Geophysics*, **53**, 50–64.
- Jin, S., 1999, Characterizing reservoir by using jointly P- and S-wave analyses: *69<sup>th</sup> Ann. Internat. Mtg., Soc. Explor. Geophys., Expanded Abstracts*, 687-690.
- Landro, M., and Veire, H. H., 2001, Joint inversion of PP- and PS-seismic data: *71<sup>st</sup> Ann. Internat. Mtg., Soc. Explor. Geophys., Expanded Abstracts*, 861-864.

- Levander, A. R., 1988, Fourth-order finite-difference P-SV seismograms: *Geophysics*, **53**, 1425–1436.
- Ostrander, W. J., 1984, Plane-wave reflection coefficients for gas sands at nonnormal angles of incidence: *Geophysics*, **49**, 1637–1648.
- Pilkington, P. E., 1988, Uses of pressure and temperature data in exploration and new developments in overpressure detection: *J. Petr. Tech.*, **40**, 543–549.
- Prasad, M., 2002, Acoustic measurements in unconsolidated sands at low effective pressure and overpressure detection: *Geophysics*, **67**, 405–412.
- Resnick, J. R., Ng, P., and Larner, K., 1987, Amplitude versus offset analysis in the presence of dip: 57<sup>th</sup> Ann. Internat. Mtg., Soc. Explor. Geophys., Expanded Abstracts, 617-620.
- Ross, C. P., and Kinman, D. L., 1995, Nonbright-spot AVO: Two examples: *Geophysics*, **60**, 1398–1408.
- Shuey, R. T., 1985, A simplification of the Zoeppritz equations: *Geophysics*, **50**, 609–614.
- Smith, G. C., and Gidlow, P. M., 1987, Weighted stacking for rock property estimation and detection of gas: *Geophys. Prosp.*, **35**, 993–1014.
- Tarantola, A., 1984, Linearized inversion of seismic data: *Geophys. Prosp.*, **32**, 998–1015.
- Villareal, A., and Scales, J. A., 1997, Distributed three-dimensional finite-difference modeling of wave propagation in acoustic media: *Computers in Physics*, **11**, 388–399.

Virieux, J., 1986, P-SV wave propagation in heterogeneous media: Velocity-stress finite-difference method: *Geophysics*, **51**, 889–901.

## VITA

### **Juan Ramon de Jesus Carcuz Jerez**

Department of Geology and Geophysics

Texas A&M University, College Station, TX 77843-3115

979-845-2400

### **Education**

M.S., May 2003, Texas A&M University, Department of Geology and Geophysics.  
Thesis: An AVO Method toward direct detection of lithologies combining  $P - P$  and  $P - S$  reflection data. Major Geophysics.

B.S., May 2001, Texas A&M University, Department of Geology and Geophysics.  
Research: Combined AVO analysis of  $P - P$  and  $P - S$  reflection data. Major Geophysics.

### **Publications**

Carcuz, J., 2001, A combined AVO analysis of  $P - P$  and  $P - S$  reflection data: 71st Ann. Internat. Mtg., Soc. Explor. Geophys., Expanded Abstracts, 323-325.

Carcuz, J. R. and Ikelle, L. T., 2003, Combining PP and PS reflection data - A method for lithology identification: 65th EAGE Conference and Exhibition, Extended Abstracts Book, P126.

### **Permanent address**

1019 Harrington, College Station, TX 77840 USA

email: juanjerez@yahoo.com

(979) 696 1107